Results in Engineering 30 (2026) 110035

Contents lists available at ScienceDirect

Results in Engineering

journal homepage: www.sciencedirect.com/journal/results-in-engineering

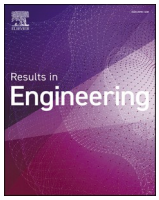

Dynamic layout optimization of truss subjected to a time-dependent load by isogeometric-analysis-based stiffness spreading method

Xiaoyan Teng [a], Lingzhi Li [a], Xudong Jiang [b,*], Haijiang Li [c]

[a] College of Mechanical and Electrical Engineering, Harbin Engineering University, NO.145 Nantong Street, Harbin 150001, Heilongjiang, China
[b] Key Laboratory of Advanced Manufacturing Intelligent Technology of Ministry of Education, Harbin University of Science and Technology, No.52 Xuefu Road, Harbin 150080, Heilongjiang, China
[c] School of Engineering, Cardiff University, Cardiff, CF24 3AA, UK

ARTICLE INFO

Keywords:
Isogeometric analysis
Stiffness spreading method
Dynamic layout optimization of truss
Proper orthogonal decomposition
Incremental singular value decomposition

ABSTRACT

An innovative and efficient truss layout optimization framework under the transient load is proposed based on the isogeometric analysis-based stiffness spreading method (IGA-based SSM), integrated with the proper orthogonal decomposition (POD). The IGA-based SSM is featured with a small number of truss elements independently moving in weak IGA background grids to represent the truss layout during optimization, without considering the connectivity of the truss elements, and hence a low computational cost due to few design variables. We use the IGA-based SSM to spread the stiffness, mass and damping matrices of a truss element to weak IGA background grids, according to energy conservation. As such, its shape and size can be simultaneously optimized during dynamic layout optimization of truss. For achieving additional savings in computational cost, the POD procedure with incremental singular value decomposition (SVD) is leveraged to reduce the primal and adjoint equations. To mitigate the consistent error in the sensitivity computation, the reduced adjoint equation is constructed based on the "discretize-then-differentiate" approach. Moreover, we tackle the computational cost and scalability of the reduced order model (ROM) learning and updating phases. Consequently, we can attain almost the same truss optimization results as the full order model (FOM), in addition to achieving high computational speed with the speedup ratio of at least 2.02 referring to FOM, which are verified by 2D and 3D benchmark problems.

1. Introduction

Truss-type load-bearing structures, due to their high stiffness-weight ratio, are widely used in engineering fields such as bridges, automotive, marine, aerospace, and aviation. With increasing requirement of large and complex equipment, how to perform the optimal layout design of truss meeting performance constraints such as the lightweight and resistance to vibration, has become one of the key challenges in the field of spatial structures. Truss layout optimization is, in essence, a discrete topology optimization of truss in the scenario of low volume fraction. For this, the ground structure method (GSM), proposed by Dorn et al. [1] and developed by Bental et al. [2] and Bendsoe et al. [3], is frequently applied owing to its simple theoretical foundations and versatility. Lai et al. [4] performed optimal truss topology by simultaneously using dual materials with different tensile and compressive properties, building upon the incorporation of BESO algorithm into GSM. Liu et al. [5] incorporated multiple types of modules to design truss structures through imposing a relaxed modular constraint for enhancing efficiency. Liu et al. [6] focused on designing hierarchical truss metastructure for desired stiffness and strength using recursive multiscale topology optimization. Sukulthanasorn et al. [7] integrated quantum annealing as a design updater to truss topology optimization. For medium and high volume fraction problems [8,9], continuum topology optimization is best suitable because it accommodates congested regions induced by converging truss bars. To achieve optimal topology containing both regions of dense and sparse structure, Lu et al. [10] proposed a hybrid truss and continuum topology optimization approach. Fairclough [11] identifies optimal truss topologies from high-resolution ground structures using the adaptive member adding strategy. Zhou et al. [12] provided a novel framework of size, shape and topology optimization for truss structure using the finite particle method, where the particle fusion and projection strategies were introduced to adjust the particle positions

* Corresponding author.
E-mail address: jxd_2023@163.com (X. Jiang).

https://doi.org/10.1016/j.rineng.2026.110035
Received 17 October 2025; Received in revised form 27 February 2026; Accepted 11 March 2026
Available online 12 March 2026

in the ground structure. Nonetheless, based on above variant versions of GSM, the resultant final truss layout is highly dependent on the initial ground structure and unsuitable for processing. To address this issue, Kozłowski et al. [13] introduced an enhanced growth method based on virtual displacements and strains fields for generating optimal design in terms of topology and geometry of truss without a generation of so-called ground structure. In the above works, the fixed connectivity assumed between truss members results in a relatively limited design space. To enlarge the design space, Wei et al. [14] proposed the stiffness spreading method (SSM), where the stiffness matrix of a truss element is projected to the weak background grids by using the radial basis function. In this way, an individual truss element is embedded in the weak background grids and can independently move there. In this context, it is unnecessary for truss elements to be connected to each other. Due to C^0 elements of conventional FEM used in the background grid of SSM, the sensitivity field is discontinuous and the numerical interpolation are inaccurate, which affect the final optimal topology of truss. In the isogeometric analysis (IGA) based FEM, the nonuniform rational B-splines (NURBS) of p-order are employed as basis functions to construct C^{p-1} continuous elements for accurate interpolation of displacement field [15]. As such, Sun et al. [16] improved the smoothness of sensitivity field and interpolation accuracy in the background grids by introducing the IGA approach to SSM. The resulting IGA-based SSM was proposed to establish the coupling relationship between truss elements and a skin represented by the weak isogeometric background grids. The IGA-based SSM demonstrates the high efficiency for the truss/stiffener topology optimization problem in the static design [16–18].

Truss structures in industrial facilities are frequently exposed to dynamic environments, wherein intense vibrations may induce structural performance deterioration [19,20]. Consequently, the dynamic topology optimization of truss structures is of substantial significance in advanced engineering applications. Conventional static topology optimization method can't capture the effect of inertia and damping on the final optimal design. Currently, dynamic topology optimization in the frequency domain has been frequently investigated. Salt et al. [21] incorporated semidefinite constraints to limit the minimal first natural frequency of pin-jointed truss structures. Ma et al. [22] minimized the peak power of the truss structure under harmonic loads with semidefinite programming. Unlike above optimization problem in frequency domain, the transient optimization problem requires repetitive primal finite element analyses for the response over a sequence of time steps and dual design sensitivity analysis during the iteration process [23,24]. The iterative computation in the primal and dual problem on the spatially and temporally discretized system significantly increases the computational burden and storage requirement. It often goes beyond the capacity of current computing platforms. To enhance the computational efficiency in dynamic topology optimization, the reduced order model (ROM) is adopted to solve primal and dual equations in the reduced space [25,26]. Modal Displacement Method (MDM) [27,28] and Modal Acceleration Method (MAM) [29] are the most extensively employed ROM based on Modal Superposition Method (MSM), where the original problem is projected onto a truncated modal space for approximation of frequency and transient responses of a structure. However, this approach fails to solve the mid- or high-frequency response due to the modal overlap effect [30]. An alternative computational technique is the series expansion method to estimate the dynamic response of a structure. The Quasi-Static Ritz Vector (QSRV), as a non-modal expansion technique, can obtain the convergent solution of a structure excited by the mid- or high-frequency load and hence applied to wide-band frequency response optimization problems [26,31]. Similarly, the second-order Krylov subspace method can efficiently and accurately solve these vibration and optimization problems [32–34]. Notably, the number of reduced basis vectors or the expansion points, and the orthogonalization algorithm of reduced basis are carefully selected for accurate estimation of the full order model (FOM). There are also several topology optimization methods based on substructuring [35] and artificial intelligence techniques [7,36–38] to improve the computational speed. Koh et al. [35] used a substructuring approach for large-scale systems in the frequency domain. Xu et al. [36] combined the Moving Morphable Component approach with Deep Neural Network for accelerating the topology optimization of serialized acoustic structures. Ma et al. [37] developed a unified computational framework by combination of an autoencoder-enhanced generative adversarial network with an elitist guidance evolutionary algorithm for dynamic optimization. Recently, Sukulthanasorn et al. [38] proposed a quantum machine learning-assisted method to speeding up density-based topology optimization by quantum neural network. In future work, an integrated approach of deep learning combined with ROM is posited as a promising technique to accelerate topology optimization problems.

Proper-orthogonal decomposition (POD) is a data-driven reduced-order modeling technique, which extract the significantly small basis functions on high-dimensional snapshots obtained from FOM to capture the most significant dynamic mode of transient problem. This data compression technique constructs low-dimensional projected space of transient analysis for the primal problem, based on the energy least-squares criterion. It has successfully been applied to structural modal prediction [39–41], flow field reconstruction [42], fluid-solid interaction of underwater vehicle [43], real-time prediction of the temperature field in the digital twin [44], etc., but not in the context of discrete topology optimization. Ke et al. [45] developed the global POD reduced-order model for geometrical design parameters by CV-Voronoi sequence sampling method, upon which vibration reduction optimization of complex thin-walled structures was performed. Xiao et al. [46] presented a projection-based reduced-order modeling approach using POD for 3D static topology optimization. Li et al. [47] proposed an efficient reanalysis framework integrated with POD-based approximate dynamic displacement strategy, which is used to construct the approximated equivalent static loads of Equivalent Static Load Method (ESLM). Nevertheless, Cao et al. [48] demonstrated that ESLM inherently produced nonnegligible errors when approximating the dynamic response sensitivity by the static response sensitivity, if the dynamic effect of problems was remarkable. Yan et al. [49] enhanced the efficient topology optimization problem in the transient heat conduction based on the Lyapunov equation and POD. In these works, the singular value decomposition (SVD) is employed to compute and store the reduced basis from simulation snapshot in a single batch in the POD framework. SVD encounters the severe challenge in computational complexity and memory requirement when dealing with a large number of high-dimensional observations.

The incremental singular value decomposition (SVD) has recently emerged in the POD framework [50]. This method treats snapshots one after the other, such that the reduced basis is on-the-fly enriched and truncated. By that means, it avoids computations on possibly redundant data, and only stores a truncated representation of the data and a single new observation. Xiao et al. [51] adaptively constructed a reduced order model by the incremental SVD for both the primal as well as dual problem in topology optimization of transient dynamic systems. However, they conducted the sensitivity analysis using the adjoint method with the "differentiate -then- discretize" approach, which might cause consistency errors, i.e., differences between the computed and exact sensitivities, as demonstrated by Jensen et al. [53] and Jiang et al. [54]. Particularly, the work of Xiao et al. is based on the continuum topology optimization method, which is suitable for medium and high volume fraction problems, whereas truss layout optimization belongs to low volume fraction problems. When employing the continuum optimization method, there are awkward issues with high resolution of truss-like layout design through the post-processing of continuum optimization and the sufficiently refined design domain problem. Furthermore, the continuum topology optimization method has to confront the difficulty in representing the hinged constraints, requiring the development of alternatives like the IGA-based SSM. The IGA-based SSM allows truss

elements independently moving in the background grids without imposing the hinged constraints. Due to modelling the background skin by high order continuous isogeometric elements, the IGA-based SSM provides the smooth sensitivity field to avoid the discontinuous sensitivity using conventional C^0 elements. To the best of the authors' knowledge, few investigations address the dynamic topology optimization of truss structures subjected to transient loads by IGA-based SSM. From the above, this study integrates the IGA-based SSM and the POD procedure with incremental SVD for efficient dynamic topology of truss structures. Regarding sensitivity analysis, we formulate the discretized adjoint equation by "discretize-then-differentiate" approach, which avoids consistency errors arising when the time-continuous adjoint equation is utilized for the transient problem. Finally, when dealing with the design case of moving loading, this work adopts a local geometry control strategy to prevent truss elements from intersection during the optimization process.

The remainder of the paper is organized as follows. Section 2 defines the transient dynamic layout optimization of truss. The IGA-based SSM is proposed to construct the coupling relationship between truss elements and a plate in the stiffness, mass and damping matrices. Section 3 develops the POD-based dynamic reduced order model of truss by incremental SVD. Section 4 formulates the primal and dual problems of truss layout optimization in the reduced space. According to the above methods, the corresponding flowchart is established to solve the transient truss layout optimization problem. Section 5 presents three numerical examples to evaluate the performance of the IGA-based SSM integrated with POD. The final conclusions are drawn in Section 6.

2. IGA-based SSM for transient dynamic layout optimization of truss

Each nodal displacement of a truss element is interpolated according to those of nine control points associated with the isogeometric plate element, where the node of the truss element is located. Hence, truss elements are assumed to be connected together, even if they don't share a common node in the IGA-based SSM, as plotted in Fig. 1.

In the global coordinate system, the stiffness and mass matrices of a truss element j, $\overline{\mathbf{K}}_{ej}$ and $\overline{\mathbf{M}}_{ej}$, are written as

$$\overline{\mathbf{K}}_{ej} = \mathbf{T}_{ej}^{\mathrm{T}} \mathbf{K}_{ej}^{*} \mathbf{T}_{ej}, \overline{\mathbf{M}}_{ej} = \mathbf{T}_{ej}^{\mathrm{T}} \mathbf{M}_{ej}^{*} \mathbf{T}_{ej} \tag{1}$$

$$\mathbf{K}_{ej}^{*} = \frac{E_{\mathrm{r}} A_j}{l_j} \begin{bmatrix} 1 & -1 \\ -1 & 1 \end{bmatrix}, \mathbf{M}_{ej}^{*} = \frac{\rho_{\mathrm{r}} A_j l_j}{6} \begin{bmatrix} 2 & 1 \\ 1 & 2 \end{bmatrix} \tag{2}$$

$$\mathbf{T}_{ej} = \begin{bmatrix} (x_{2j-1} - x_{2j})/l_j & \left(y_{2j-1} - y_{2j}\right)/l_j & 0 & 0 \\ 0 & 0 & (x_{2j-1} - x_{2j})/l_j & \left(y_{2j-1} - y_{2j}\right)/l_j \end{bmatrix} \tag{3}$$

where $\mathbf{K}_{ej}^{*}$ and $\mathbf{M}_{ej}^{*}$ are the stiffness and mass matrices of a truss element j in the local coordinate system, E_{r} and ρ_{r} are the Young's modulus and physical density, A_j and l_j are the cross-sectional area and the length of a truss element j, and $\mathbf{T}_{ej}$ is defined as the transformation matrix.

To integrate the stiffness and inertial contribution of the jth truss element stiffness and mass matrices ($\overline{\mathbf{K}}_{ej}$, $\overline{\mathbf{M}}_{ej}$) into the IGA background grids, the spreading stiffness and mass matrices of this truss element ($\mathbf{K}_{ej}^{+}$, $\mathbf{M}_{ej}^{+}$) are constructed in the light of the following energy conservation relationships.

$$\mathbf{u}_{ej}^{\mathrm{T}} \mathbf{K}_{ej}^{+} \mathbf{u}_{ej} = \mathbf{u}_{rj}^{\mathrm{T}} \overline{\mathbf{K}}_{ej} \mathbf{u}_{rj}, \dot{\mathbf{u}}_{ej}^{\mathrm{T}} \mathbf{M}_{ej}^{+} \dot{\mathbf{u}}_{ej} = \dot{\mathbf{u}}_{rj}^{\mathrm{T}} \overline{\mathbf{M}}_{ej} \dot{\mathbf{u}}_{rj} \tag{4}$$

where $\mathbf{u}_{rj}$ and $\dot{\mathbf{u}}_{rj}$ are the displacement and velocity vectors of the jth truss element, $\mathbf{u}_{ej}$ and $\dot{\mathbf{u}}_{ej}$ are the displacement and velocity vectors of control points corresponding to the isogeometric element in the IGA background grids.

Substituting the interpolation equation, $\mathbf{u}_{rj} = \mathbf{N}\mathbf{u}_{ej}$ to Eqs. (4) and (5), the spreading stiffness and mass matrices of the truss element can be obtained as follows, respectively,

$$\mathbf{K}_{ej}^{+} = \mathbf{N}^{\mathrm{T}} \overline{\mathbf{K}}_{ej} \mathbf{N}, \mathbf{M}_{ej}^{+} = \mathbf{N}^{\mathrm{T}} \overline{\mathbf{M}}_{ej} \mathbf{N} \tag{5}$$

where $\mathbf{N}$ is the IGA basis function matrix.

By assembling the spreading stiffness and mass matrices of truss elements to those of the IGA background grids, the global stiffness and mass matrices are expressed as,

$$\mathbf{K} = \mathbf{K}_p + \sum_{j}^{n} \mathbf{K}_{ej}^{+}, \mathrm{M} = \mathbf{M}_p + \sum_{j}^{n} \mathbf{M}_{ej}^{+} \tag{6}$$

where $\mathbf{K}_p$ and $\mathbf{M}_p$ are the global stiffness and mass matrices, respectively, and n is the total number of truss elements. $\mathbf{K} \in \mathbf{R}^{(d\cdot\overline{n})\times(d\cdot\overline{n})}$ and $\mathrm{M} \in \mathbf{R}^{(d\cdot\overline{n})\times(d\cdot\overline{n})}$ are the respective global stiffness and mass matrices, where $\overline{n}$ denotes the total number of control points in the background grids and d the number of DOF of every control point with $d = 2$ for 2D background grids and $d = 3$ for 3D background grids in this work.

Following a standard FE procedure, the elastodynamic boundary value problem for the compound truss structure adopts the form,

$$\mathbf{M}\ddot{\mathbf{u}}_t + \mathbf{C}\dot{\mathbf{u}}_t + \mathbf{K}\mathbf{u}_t = \mathbf{f}_t t = 0, \cdots, \overline{N} \tag{7}$$

where $\mathbf{f}_t$ is the external force vector at the tth time step, and $\overline{N}$ is the number of the time steps, and $\ddot{\mathbf{u}}_t$, $\dot{\mathbf{u}}_t$ and $\mathbf{u}_t$ are, respectively, the acceleration, velocity, and displacement vectors at the tth time step, and $\mathbf{C} \in \mathbf{R}^{(d\cdot\overline{n})\times(d\cdot\overline{n})}$ is the global damping matrix. We calculate the damping matrix by linear combination of $\mathbf{M}$ and $\mathbf{K}$, written as:

$$\mathbf{C} = \alpha_r \mathbf{M} + \beta_r \mathbf{K} \tag{8}$$

where α_r and β_r are the proportional coefficients in the Rayleigh damping model.

The dynamic stiffness maximization problem is physically equivalent to the dynamic compliance minimization problem, since the dynamic stiffness can be defined as the inverse measure of dynamic compliance under transient loading. Therefore, maximizing dynamic stiffness leads

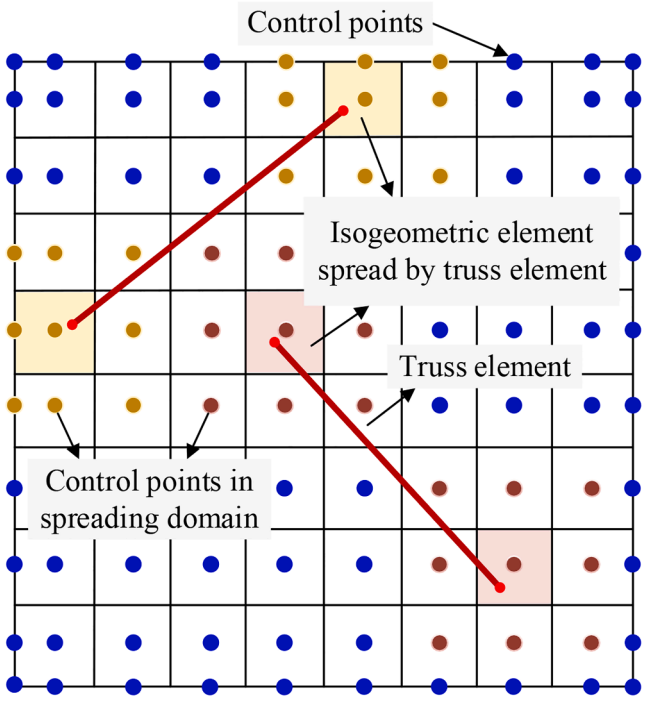

Fig. 1. Schematic diagram of IGA-based SSM.

to minimizing the structural dynamic compliance, and vice versa. By IGA-based SSM, we formulate the transient dynamic layout optimization of truss for dynamic stiffness maximization as:

$$\begin{aligned}
&\min f\left(x_{2j-1}, x_{2j}, y_{2j-1}, y_{2j}, A_j, \mathbf{u}_0, \ldots, \mathbf{u}_{\overline{N}}\right) = 1/\overline{N}\sum_{t=0}^{\overline{N}} \mathbf{F}_t^{\mathrm{T}}\mathbf{u}_t \\
&\text{s.t.}\mathbf{M}\ddot{\mathbf{u}}_t + \mathbf{C}\dot{\mathbf{u}}_t + \mathbf{K}\mathbf{u}_t = \mathbf{f}_t, t = 1, \cdots, \overline{N} \\
&G = \sum_{j=1}^{n} A_j l_j - V_{\max} \le 0 \\
&\begin{aligned} x_{\min} \le x_{2j-1}, x_{2j} \le x_{\max} \\ y_{\min} \le y_{2j-1}, y_{2j} \le y_{\max} \end{aligned} \; j = 1, 2, \cdots, n
\end{aligned} \tag{9}$$

where $\begin{bmatrix} x_{2j-1} & x_{2j} & y_{2j-1} & y_{2j} & A_j \end{bmatrix}$ (j = 1, 2, …, n) represent all design variables, and n is the total number of truss elements. $V_{\max}$ is the upper bound of the total volume of truss elements. Here, the optimization problem (9) is oriented towards a time-dependent field dominated by full order model (FOM).

3. POD-based reduced order model

In order to reduce the computational cost of Eq. (9), we construct a reduced basis $\mathbf{\Phi}$ based on a set of snapshots for the displacement field $\mathbf{S}_u = [\mathbf{u}_1, \mathbf{u}_2, \cdots, \mathbf{u}_{\overline{N}}]$, where $\mathbf{u}_i$ is the full-order solution of Eq. (7) at the ith time step. The reduced basis is optimally obtained using proper orthogonal decomposition (POD) through the solution of a least-squares problem and subsequentially the approximation of $\mathbf{u}(t)$, namely $\mathbf{u}^{\mathrm{app}}(t)$, is expressed as a linear combination of basis vectors:

$$\mathbf{u}(t) \approx \mathbf{u}^{\mathrm{app}}(t) = \mathbf{\Phi}\theta(t) \tag{10}$$

where $\mathbf{\Phi} \in R^{N \times N_b}$, N_b is the number of reduced basis vectors and N is the degrees of freedom (DOF) of FOM, generally $N_b \ll N$. $\boldsymbol{\theta}(t) \in R^{N_b \times 1}$ is the coefficient vector of POD basis at the time step t. Due to the independence of $\mathbf{\Phi}$ from the time, the approximate velocity and acceleration are, respectively, rewritten as:

$$\dot{\mathbf{u}}(t) \approx \dot{\mathbf{u}}^{\mathrm{app}}(t) = \mathbf{\Phi}\dot{\theta}(t), \ddot{\mathbf{u}}(t) \approx \ddot{\mathbf{u}}^{\mathrm{app}}(t) = \mathbf{\Phi}\ddot{\theta}(t) \tag{11}$$

Through substitution of Eqs. (10) and (11) into Eq. (7), and following Galerkin projection, the Eq. (7) is rewritten as

$$\widehat{\mathbf{M}}\ddot{\theta}(t) + \widehat{\mathbf{C}}\dot{\theta}(t) + \widehat{\mathbf{K}}\theta(t) = \widehat{\mathbf{F}}(t) \tag{12}$$

where

$$\begin{aligned}
&\widehat{\mathbf{M}} = \mathbf{\Phi}^{\mathrm{T}}\mathbf{M}\mathbf{\Phi}, \widehat{\mathbf{C}} = \mathbf{\Phi}^{\mathrm{T}}\mathbf{C}\mathbf{\Phi} \\
&\widehat{\mathbf{K}} = \mathbf{\Phi}^{\mathrm{T}}\mathbf{K}\mathbf{\Phi}, \widehat{\mathbf{F}}(t) = \mathbf{\Phi}^{\mathrm{T}}\mathbf{F}(t)
\end{aligned} \tag{13}$$

$\widehat{\mathbf{M}}, \widehat{\mathbf{K}}, \widehat{\mathbf{C}} \in \mathbf{R}^{r \times r}$ are the reduced system matrices and r is the optimal number of POD bases.

From this, the original full-order equation of (7) with N DOF is transformed into the reduced-order equation of (12) with N_b DOF. For convenience, $\boldsymbol{\theta}(t)$ and $\widehat{\mathbf{F}}(t)$ are abbreviated as $\boldsymbol{\theta}_t$ and $\widehat{\mathbf{F}}_t$ in the later sections. Similar abbreviation is adopted for other time-dependent variables. Once the above reduced linear system is solved, the resulting solution $\boldsymbol{\theta}_t$ is pulled back to the FE solution $\mathbf{u}_t^{\mathrm{app}}$.

To solve the reduced-order motion equation of the Eq. (12), we use the HHT-α method (Chung et al. [52]), which is an extension of the Newmark-β method. This HHT-α algorithm is also employed to solve the full-order motion equation of the Eq. (7) for the snapshots of all moments in time. The HHT-α method adjusts the reduced motion equation of (12) by a parameter α denoting a numerical delay among the damping, stiffness, and external force vector, expressed as:

$$\widehat{\mathbf{M}}\ddot{\theta}_t + (1-\alpha)\widehat{\mathbf{C}}\dot{\theta}_t + \alpha\widehat{\mathbf{C}}\dot{\theta}_{t-1} + (1-\alpha)\widehat{\mathbf{K}}\boldsymbol{\theta}_t + \alpha\widehat{\mathbf{K}}\boldsymbol{\theta}_{t-1} = (1-\alpha)\widehat{\mathbf{F}}_t + \alpha\widehat{\mathbf{F}}_{t-1} \tag{14}$$

We evaluate $\boldsymbol{\theta}_t$ and $\dot{\theta}_t$ using the Newmark-β finite difference (FD) relationships, as follows:

$$\begin{aligned}
&\boldsymbol{\theta}_t = \boldsymbol{\theta}_{t-1} + \Delta t\dot{\theta}_{t-1} + \Delta t^2\left[\left(\frac{1}{2}-\beta\right)\ddot{\theta}_{t-1} + \beta\ddot{\theta}_t\right] \\
&\dot{\theta}_t = \dot{\theta}_{t-1} + \Delta t\left[(1-\gamma)\ddot{\theta}_{t-1} + \gamma\ddot{\theta}_t\right]
\end{aligned} \tag{15}$$

where $0 \le \alpha \le 1/3$, $\beta = (1+\alpha)^2/4$ and $\gamma = (1+2\alpha)/2$ must be satisfied to ensure the HHT-α method with at least second-order accuracy and unconditional stability.

Substituting the Newmark-β FD relationships (15) into (14), the corresponding residual form can be obtained as:

$$\widehat{\mathbf{R}}_t = \widehat{\mathbf{M}}_1\ddot{\theta}_t + \widehat{\mathbf{M}}_0\ddot{\theta}_{t-1} + \widehat{\mathbf{C}}_0\dot{\theta}_{t-1} + \widehat{\mathbf{K}}\ddot{\theta}_{t-1} - (1-\alpha)\widehat{\mathbf{F}}_t - \alpha\widehat{\mathbf{F}}_{t-1} = \mathbf{0} \tag{16}$$

where

$$\begin{aligned}
&\widehat{\mathbf{M}}_1 = \widehat{\mathbf{M}} + (1-\alpha)\gamma\Delta t\widehat{\mathbf{C}} + (1-\alpha)\beta\Delta t^2\widehat{\mathbf{K}} \\
&\widehat{\mathbf{M}}_0 = (1-\alpha)(1-\gamma)\Delta t\widehat{\mathbf{M}} + (1-\alpha)\left(\frac{1}{2}-\beta\right)\Delta t^2\widehat{\mathbf{K}} \\
&\widehat{\mathbf{C}}_0 = \widehat{\mathbf{C}} + (1-\alpha)\Delta t\widehat{\mathbf{K}}
\end{aligned} \tag{17}$$

For $t = 0$, the residual form of the HHT-α method from (13) together with the initial condition is formulated as:

$$\widehat{\mathbf{R}}_0 = \widehat{\mathbf{M}}\ddot{\theta}_0 + \widehat{\mathbf{C}}\dot{\theta}_0 + \widehat{\mathbf{K}}\boldsymbol{\theta}_0 - \widehat{\mathbf{F}}_0 = \mathbf{0} \tag{18}$$

where

$$\boldsymbol{\theta}_0 = \mathbf{\Phi}^{\mathrm{T}}\mathbf{u}_0 \tag{19}$$

As is known, the above reduced linear system is solved by HHT-α method and hence the low-dimensional approximation $\mathbf{u}_t^{\mathrm{app}}$ can be obtained. In Appendix A, we demonstrate how to deduce the optimal POD bases from the resultant snapshot matrix.

4. Primal–dual reduced-order modeling of truss layout optimization

As illustrated in Section 3, we solve the primal equation represented by FOM and then sample $\overline{N}$ snapshots uniformly in the time duration. The primal truss layout optimization is reduced as the time-dependent problem of low-dimensional representation, i.e.

$$\begin{aligned}
&\min f^{\mathrm{app}}\left(x_{2j-1}, x_{2j}, y_{2j-1}, y_{2j}, A_j, \boldsymbol{\theta}_0, \cdots, \boldsymbol{\theta}_{\overline{N}}\right) = 1/\overline{N}\sum_{t=0}^{\overline{N}} \mathbf{F}_t^{\mathrm{T}}\mathbf{u}_t^{\mathrm{app}} \\
&\text{s.t.}\widehat{\mathbf{M}}\ddot{\theta}_t + \widehat{\mathbf{C}}\dot{\theta}_t + \widehat{\mathbf{K}}\boldsymbol{\theta}_t = \widehat{\mathbf{F}}_t, t = 1, \cdots, \overline{N} \\
&\mathbf{u}_t^{\mathrm{app}} = \mathbf{\Phi}\boldsymbol{\theta}_t \\
&G = \sum_{j=1}^{n} A_j l_j - V_{\max} \le 0 \\
&\begin{aligned} x_{\min} \le x_{2j-1}, x_{2j} \le x_{\max} \\ y_{\min} \le y_{2j-1}, y_{2j} \le y_{\max} \end{aligned} \; j = 1, 2, \cdots, n
\end{aligned} \tag{20}$$

where the primal objective function $f\left(x_{2j-1}, x_{2j}, y_{2j-1}, y_{2j}, A_j, \mathbf{u}_0, \ldots, \mathbf{u}_{\overline{N}}\right)$, is explicitly estimated as $f^{\mathrm{app}}\left(x_{2j-1}, x_{2j}, y_{2j-1}, y_{2j}, A_j, \boldsymbol{\theta}_0, \cdots, \boldsymbol{\theta}_{\overline{N}}\right)$, abbreviated as f^{app}.

4.1. Sensitivity analysis on the reduced order model

In order to avoid the expensive computation of derivatives of the state variables, we employ the adjoint method for computationally efficient sensitivity analysis. Two main strategies are dominant for the adjoint sensitivity analysis of transient problem. One is the

"differentiate-then-discretize" method where the adjoint problem is built in the semi-discretized system represented by the space- discretization and time-continuous state variables, (Ramírez-Gil et al. [24], Li et al. [27], Zhu et al. [28], Wang et al. [31], Long et al. [33] and Xiao et al. [51]). Alternative is the "discretize-then-differentiate" method where the adjoint problem is built in the spatio-temporally discretized system, (Oliver et al. [23] and Kristiansen et al. [34]). Though the former is simply implemented, Jensen et al. [53] and Jiang et al. [54] indicate that the "differentiate-then-discretize" method inherently produces the consistent errors for the transient problem, namely differences between the calculated and accurate sensitivities. As a result, we choose the latter "discretize-then-differentiate" method to consistently evaluate the sensitivity.

We introduce the Lagrange multiplier $\boldsymbol{\lambda}_t$, $\boldsymbol{\mu}_t$ and $\boldsymbol{\xi}_t$, $t = 1, \cdots, \overline{N}$ as the adjoint or dual variables and the sensitivity of the objective function f^{app}, with regard to a design variable $S_j \in \begin{bmatrix} x_{2j-1} & x_{2j} & y_{2j-1} & y_{2j} & A_j \end{bmatrix}$, is written as:

$$\frac{\mathrm{d}f^{\text{app}}}{\mathrm{d}S_j} = \frac{\partial f^{\text{app}}}{\partial S_j} + \sum_{t=0}^{\overline{N}} \frac{\partial f^{\text{app}}}{\partial \boldsymbol{\theta}_t}\frac{\partial \boldsymbol{\theta}_t}{\partial S_j} + \sum_{t=1}^{\overline{N}} \boldsymbol{\lambda}_t^{\mathrm{T}}\frac{\mathrm{d}\widehat{\mathbf{R}}_t}{\mathrm{d}S_j} + \sum_{t=1}^{\overline{N}} \boldsymbol{\mu}_t^{\mathrm{T}}\frac{\mathrm{d}\widehat{\mathbf{P}}_t}{\mathrm{d}S_j} + \sum_{t=1}^{\overline{N}} \boldsymbol{\xi}_t^{\mathrm{T}}\frac{\mathrm{d}\widehat{\mathbf{Q}}_t}{\mathrm{d}S_j} \tag{21}$$

where $\widehat{\mathbf{P}}_t$ and $\widehat{\mathbf{Q}}_t$ denote the residual form of the Newmark-β FD relationships (15), and are rewritten as:

$$\begin{aligned} \widehat{\mathbf{P}}_t &= -\boldsymbol{\theta}_t + \boldsymbol{\theta}_{t-1} + \Delta t\dot{\boldsymbol{\theta}}_{t-1} + \Delta t^2\left[(0.5-\beta)\ddot{\boldsymbol{\theta}}_{t-1} + \beta\ddot{\boldsymbol{\theta}}_t\right] = \mathbf{0} \\ \widehat{\mathbf{Q}}_t &= -\dot{\boldsymbol{\theta}}_t + \dot{\boldsymbol{\theta}}_{t-1} + \Delta t\left[(1-\gamma)\ddot{\boldsymbol{\theta}}_{t-1} + \gamma\ddot{\boldsymbol{\theta}}_t\right] = \mathbf{0} \end{aligned} \tag{22}$$

To eliminate all terms including $\partial\ddot{\boldsymbol{\theta}}_t/\partial S_i$, $\partial\dot{\boldsymbol{\theta}}_t/\partial S_i$ and $\partial\boldsymbol{\theta}_t\ /\partial S_i$in Eq. (21), the adjoint or dual problem is defined as: for $t = 0$,

$$\boldsymbol{\lambda}_0^{\mathrm{T}}\frac{\partial\widehat{\mathbf{R}}_0}{\partial\ddot{\boldsymbol{\theta}}_0} + \boldsymbol{\lambda}_1^{\mathrm{T}}\frac{\partial\widehat{\mathbf{R}}_1}{\partial\ddot{\boldsymbol{\theta}}_0} + \boldsymbol{\mu}_1^{\mathrm{T}}\frac{\partial\widehat{\mathbf{P}}_1}{\partial\ddot{\boldsymbol{\theta}}_0} + \boldsymbol{\xi}_1^{\mathrm{T}}\frac{\partial\widehat{\mathbf{Q}}_1}{\partial\ddot{\boldsymbol{\theta}}_0} = \mathbf{0} \tag{23}$$

for $t = 1, \cdots, \overline{N}$,

$$\begin{aligned} &\sum_{\ell=1}^{\overline{N}}\left(\boldsymbol{\lambda}_\ell^{\mathrm{T}}\frac{\partial\widehat{\mathbf{R}}_\ell}{\partial\boldsymbol{\theta}_t} + \boldsymbol{\mu}_\ell^{\mathrm{T}}\frac{\partial\widehat{\mathbf{P}}_\ell}{\partial\boldsymbol{\theta}_t} + \boldsymbol{\xi}_\ell^{\mathrm{T}}\frac{\partial\widehat{\mathbf{Q}}_\ell}{\partial\boldsymbol{\theta}_t} + \frac{\partial f^{\text{app}}}{\partial\boldsymbol{\theta}_t}\right) = \mathbf{0} \\ &\sum_{\ell=1}^{\overline{N}}\left(\boldsymbol{\lambda}_\ell^{\mathrm{T}}\frac{\partial\widehat{\mathbf{R}}_\ell}{\partial\dot{\boldsymbol{\theta}}_t} + \boldsymbol{\mu}_\ell^{\mathrm{T}}\frac{\partial\widehat{\mathbf{P}}_\ell}{\partial\dot{\boldsymbol{\theta}}_t} + \boldsymbol{\xi}_\ell^{\mathrm{T}}\frac{\partial\widehat{\mathbf{Q}}_\ell}{\partial\dot{\boldsymbol{\theta}}_t}\right) = \mathbf{0} \\ &\sum_{\ell=1}^{\overline{N}}\left(\boldsymbol{\lambda}_\ell^{\mathrm{T}}\frac{\partial\widehat{\mathbf{R}}_\ell}{\partial\ddot{\boldsymbol{\theta}}_t} + \boldsymbol{\mu}_\ell^{\mathrm{T}}\frac{\partial\widehat{\mathbf{P}}_\ell}{\partial\ddot{\boldsymbol{\theta}}_t} + \boldsymbol{\xi}_\ell^{\mathrm{T}}\frac{\partial\widehat{\mathbf{Q}}_\ell}{\partial\ddot{\boldsymbol{\theta}}_t}\right) = \mathbf{0} \end{aligned} \tag{24}$$

from which we can compute the sensitivity of the objective function as:

$$\frac{\mathrm{d}f^{\text{app}}}{\mathrm{d}S_j} = \frac{\partial f^{\text{app}}}{\partial S_j} + \sum_{t=0}^{\overline{N}}\boldsymbol{\lambda}_t^{\mathrm{T}}\frac{\partial\widehat{\mathbf{R}}_t}{\partial S_j} \tag{25}$$

Further details about this sensitivity analysis procedure are given in Appendix B.

Finally, the convergence criterion is written as

$$\frac{\left|\sum_{I=1}^{\text{IN}}\left[f_{t-I+1}^{\text{app}} - f_{t-I}^{\text{app}}\right]\right|}{\text{IN}} < \xi \tag{26}$$

where IN is an integral number, t and ξ denotes the respective current iteration counter and the allowable error.

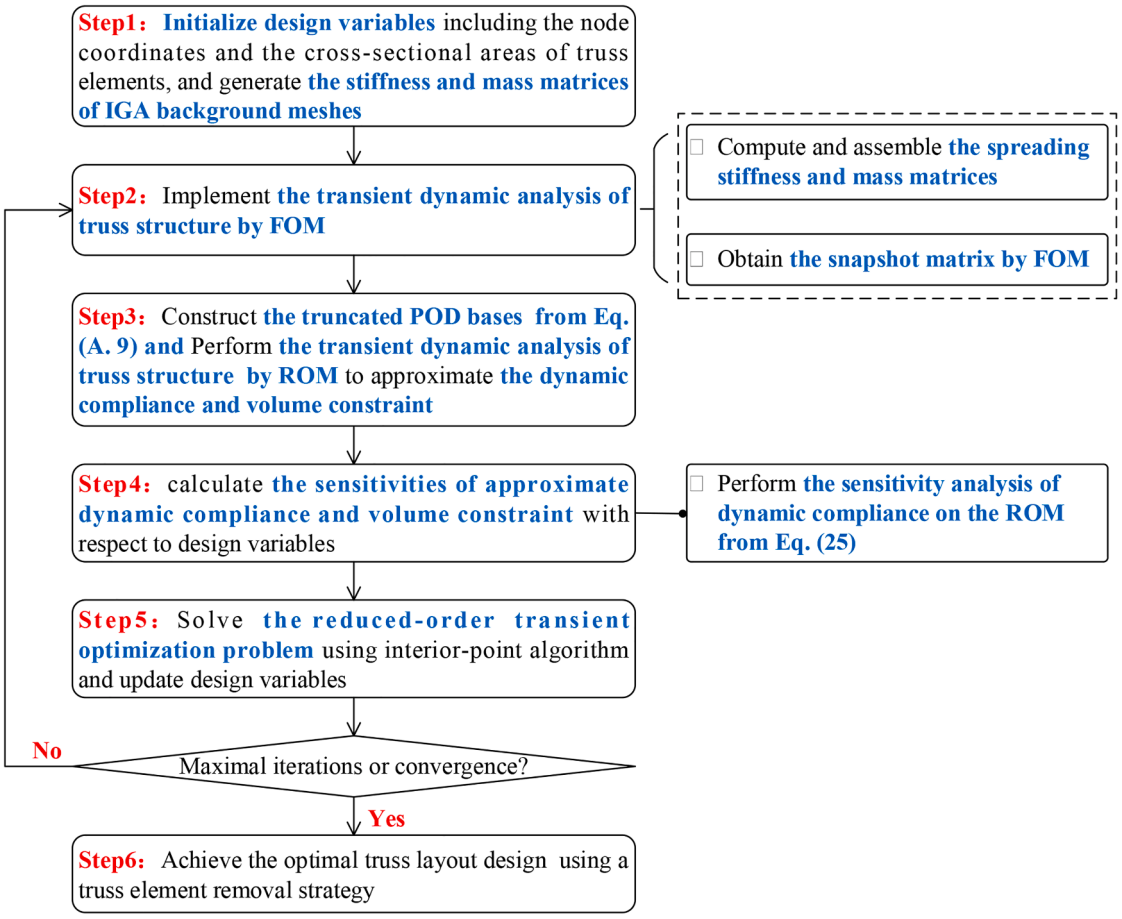

Fig. 2. Flowchart of truss layout optimization by primal–dual reduced-order modeling.

4.2. Flowchart of truss layout optimization

The flowchart of the IGA-based SSM for the dynamic compliance minimization problem of truss layout is illustrated in Fig. 2 and the steps are as follows.

Step 1: Design variables, including the nodal coordinates, the cross-sectional area of truss elements, are initialized for dynamic transient truss layout optimization. The isogeometric background meshes are developed and their stiffness and mass matrices are computed and stored, respectively.

Step 2: The spreading stiffness and mass matrices of truss elements are obtained by IGA-based SSM and assembled in terms of the corresponding control point numbering of background meshes. The full-order isogeometric analysis of the compound truss is implemented for acquiring the snapshot matrix across the time duration.

Step 3: According to the obtained snapshot matrix, the truncated POD bases are constructed and real-time updated by incremental SVD. Then the reduced-order isogeometric model of the compound truss is established such that the approximate dynamic compliance is evaluated through a linear elastodynamic analysis. The volume constraint is also computed.

In this step, the POD bases are constructed by traversing the snapshots at all specified moments. Once the residual between a snapshot and its projection exceeds the prescribed tolerance, the POD bases must be updated according to Eq. (A.7). The truncated POD bases are obtained from Eq. (A.9).

Step 4: Based on the adjoint method with the "discretize-then-differentiate" strategy, the sensitivity analysis is consistently performed on the reduced-order isogeometric model of the compound truss. The sensitivities of approximate dynamic compliance and volume constraint regarding design variables are obtained.

Step 5: The interior-point algorithm (Waltz et al. [55]) is utilized to solve the reduced-order transient optimization problem for minimizing the dynamic compliance of the compound truss. The design variables are updated until the maximum number of iterations or the convergence criteria is attained.

Step 6: A simple truss element removal strategy (Sun et al. [16]) is used to achieve clear truss optimal layout results while the optimized cross-sectional area is less than a specified threshold, i.e., $A \leq 0.01A_{\max}$, or the optimized truss length is less than a specified infimum, i.e., $l \leq 0.01l_{\max}$. Here, $A_{\max}$ and $l_{\max}$ are the maximal cross-sectional area and truss length in the final design.

5. Numerical examples

This section presents 2D and 3D numerical examples to illustrate the performance of the IGA-based SSM combined with POD for dynamic transient truss layout optimization. The outcomes are assessed from two aspects. The first is the accuracy of ROM in the transient solution across the time duration. This evaluation is concerned with the capability of ROM to efficiently yield accurate solution. The second is how the POD influences the optimization processes, which are indexed to the reduction in CPU execution time, as a lower amount of POD bases is exploited. Moreover, the effect of increasing the tolerance updating the POD basis on the optimal result, and the CPU utilization are discussed in detail.

To ensure the sensitivity continuous and smooth in the context of IGA-based SSM, the order of the NURBS basis function is set as 2. The elastic modulus and mass density of the truss element are 1000 times as large as those of the background grids. The elastic modulus and mass density of the truss elements are $E_r = 200\text{GPa}$ and $\rho_r = 7800\text{kg/m}^3$, and both the truss elements and the background grids have the same Poisson's ratio, $\mu = 0.3$. The Rayleigh damping parameters of the truss are set as follows: $\alpha_r = 10\text{s}^{-1}$ and $\beta_r = 10^{-5}\text{s}$. The allowed convergence error ξ, the integral IN, and the maximal iteration number are specified to be 0.001, 10, and 1400. Furthermore, we use $\alpha = 0.05$, $\beta = (1+\alpha)^2/4$, $\gamma = (1+2\alpha)/2$ in all examples, to ensure unconditional stability and minimal second-order accuracy of the HHT-α method.

5.1. 2D simply supported beam design under rectangular pulse load

This example optimizes a simply supported beam to discuss the influence of time interval on the final designs. As plotted in Fig. 3, the design domain is a simply supported beam under the rectangular pulse load imposed at the center of the above free edge. The amplitude of the transient load f_0 is 10 kN and the pulse width τ_1 is 0.005 s, while the pulse intervalτ_2 is specified as 0.002 s, 0.004 s and 0.008 s. This beam has the length of $L = 48\text{m}$, the height of $H = 8\text{m}$, and the thickness of $h = 0.1\text{m}$. The background domain is discretized into 24×4 isogeometric plane stress elements with 26×6 control points. Each control point has two degrees of freedom, namely the displacements along the x and y directions. The total number of time steps is $\overline{N} = 100$ with the time step, $\Delta t = 0.18\text{ms}$ and the specified tolerance for on-the-fly basis update is $e_b = 10^{-5}$.

Fig. 4 shows the initial layout and three optimal designs of the truss, which are obtained for $\tau_2 = 0.002\text{s}$, $\tau_2 = 0.004\text{s}$ and $\tau_2 = 0.008\text{s}$, respectively. The optimal results are based on the least POD bases, $r = 4$. As seen in Fig. 4b, the final layouts are sensitive to τ_2. When the external load is imposed at a faster rate, the optimizer places less material around the load application point while more material towards both simply supported edges. It is attributed to the fact that such material distribution enables effective suppression of the increased local deformation around the load application point, which occurs owing to the increasing transient effects. Fig. 5 shows the iteration history of the objective function for both FOM and ROM. The iteration history illustrates a stable decrease in the objective function during the optimization process.

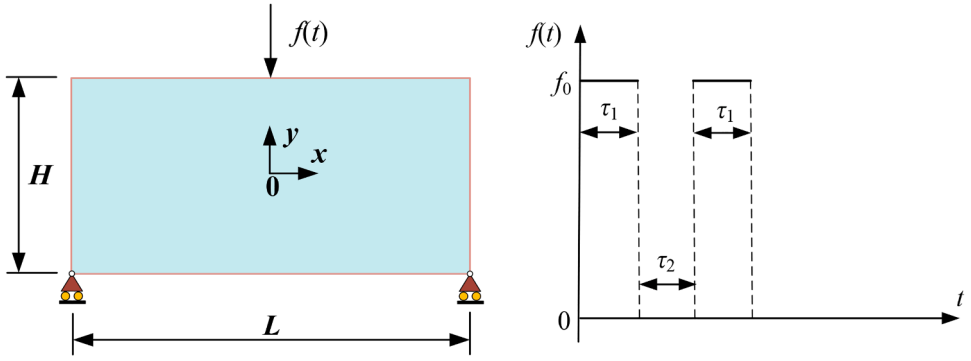

Fig. 3. Problem setup for the 2D simply supported beam.

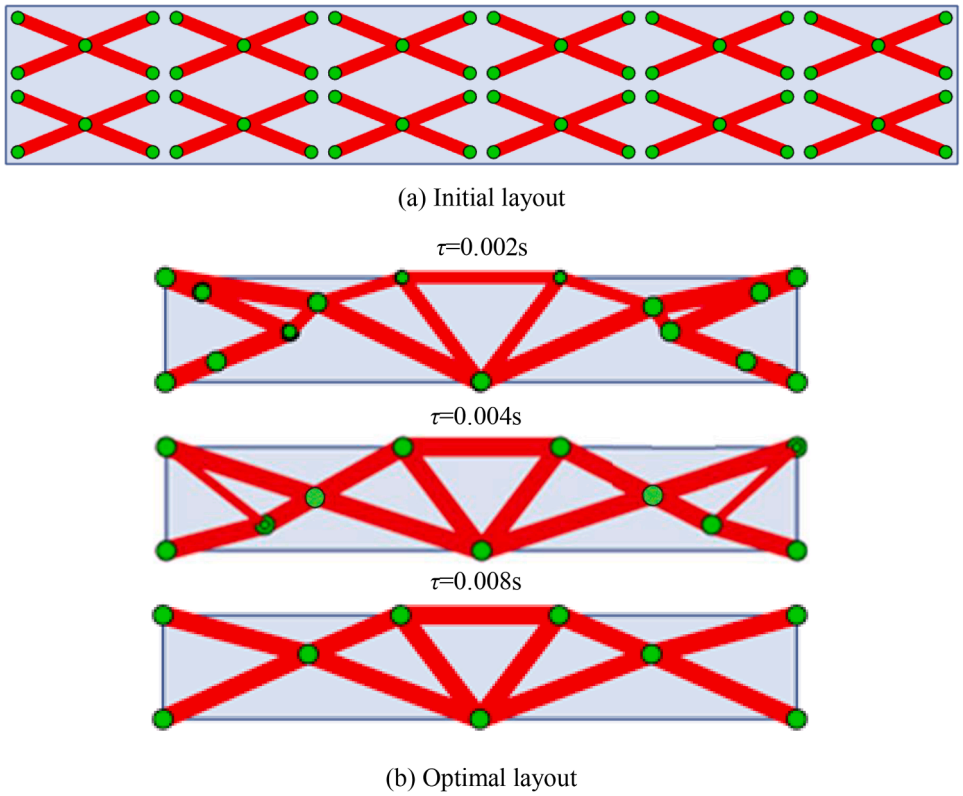

Fig. 4. Optimized truss layout for the 2D simply supported beam problem.

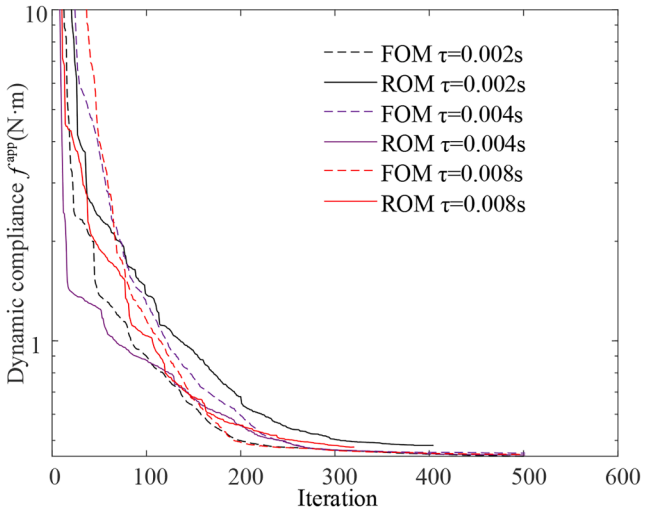

Fig. 5. Convergent histories for the 2D simply supported beam.

Particularly, the optimized layouts obtained by ROM are identical to those obtained by FOM, as shown in Fig. 4b

To analyze the effect of different basis size, we retain the previous settings for the other parameters while vary the POD bases size N_b as 4, 8, 10,15 and 18. The results for each scenario is listed in Table 1. Table 1 compares the results of classical topology optimization (the first row) with those obtained from POD-based optimizations under different N_b. The "CPU running time" column (the third column) indicates the total time throughout the optimization for both FOM and ROM, while the "speedup ratio" (the fourth column) is the ratio of the CPU running time by the FOM to that by the ROM. The latter can directly measure the relative acceleration performance of ROM iterations for the optimization duration. The "memory requirement" column (the sixth column) provides a clear understanding of the discrete system size to estimate storage demands.

In contrast to the FOM, the ROM consumes remarkably less computational time and hence speeds up optimization process. Also, all optimal results are closely consistent with those from the FOM maintaining the relative high precision. As demonstrated in Fig. 6, when the POD bases size N_b is merely set as 4, the vertical displacement at the load application point, obtained by the ROM is sufficiently precise, which explains why ROM and FOM share the almost same optimized results. With increasing N_b, the acceleration ratio of the proposed algorithm based on ROM declines, though the precision retains stable. Accordingly, we recommend to choose smaller N_b to attain a trade-off between computational cost and accuracy. This example suggests that the preferred N_b ranging from 4 to 10 achieving the relative error of 1.2 %

Table 1
Performance comparison between FOM and ROM with various N_b in optimal layout design of 2D simply supported beam for the case of τ_2=0.004 s.

Method	N_b	CPU running time/s	Speedup ratio	Optimal dynamic compliance/Nm	Memory requirement/Mb	Relative errors in optimal objective
FOM	-	1921.4	1.00	4.5787	1014.16	-
ROM	4	381.3	5.04	4.5211	35.72	1.2 %
	8	654.1	2.94	4.5573	-	0.5 %
	10	952.1	2.02	4.5805	-	0.04 %
	15	1452.6	1.32	4.5785	-	0.004 %
	18	1783.2	1.08	4.5785	-	0.004 %

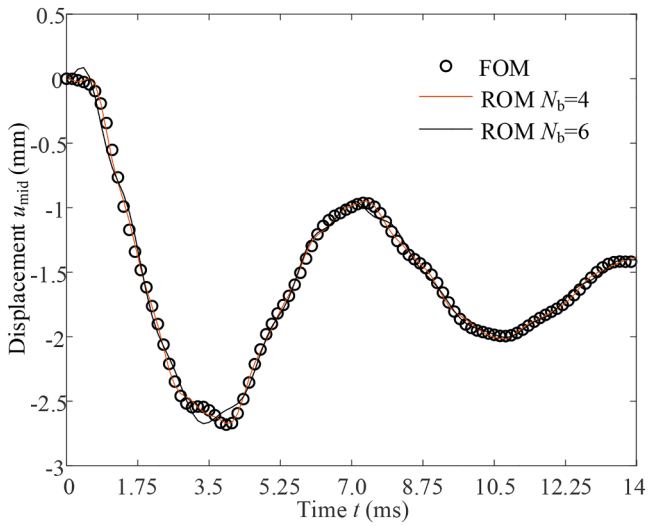

Fig. 6. Time histories of vertical displacement at the load application point for the 2D simply supported beam.

~0.04 % and the speed ratio of 5.04~2.02. Actually, the minimal preferred number of POD bases is calculated as 4 from the inequality (A.8). Obviously, the ROM has much lower memory requirement than the FOM, as listed in Table 1.

5.2. Spatial cantilever beam design under half-cycle cosine load

We use this example to furtherly validate the feasibility of the proposed approach for a spatial truss transient layout optimization problem. A similar 3D beam is fixed at two vertical edges of the left surface and loaded vertically with a half-cycle cosine load imposed at the center of the right surface, as shown in Fig. 7. The amplitude of the transient load f_0 is 10 kN and the time duration is 0.1 s. The 3D beam has length, L = 10m, width, W = 10m, Height H = 10m. The background grids are meshed by 10×10×10 isogeometric solid elements with 12×12×12 control points. Each control point has three degrees of freedom, namely the displacements along the *x, y* and *z* directions. The number of sampling time step is $\overline{N} = 100$ with the time step, Δt = 1.0msand the prescribed tolerance for on-the-fly basis update is $e_b = 10^{-6}$.

The initial and optimal truss layouts for the 3D cantilever beam are shown in Fig. 8., Fig. 9 plots the iteration history for the 3D layout design problem. The results of the iterations show that the stable convergence has been attained for both ROM of N_b = 4and FOM approaches. The final optimized results with ROM and FOM are almost the same.

Additionally, this example examines the influence of varying tolerance for basis update on optimization results and algorithm performance. Keeping N_b = 4, the tolerance for basis update is specified to be 10^{-2}, 10^{-4} and 10^{-6}, respectively. Table 4 indicates that the tolerance for basis update regulates the precision of ROMs. As selecting large tolerances for basis update, ROM yields different optimal outcomes compared with FOM. The achieved precision is within the range of 0.07

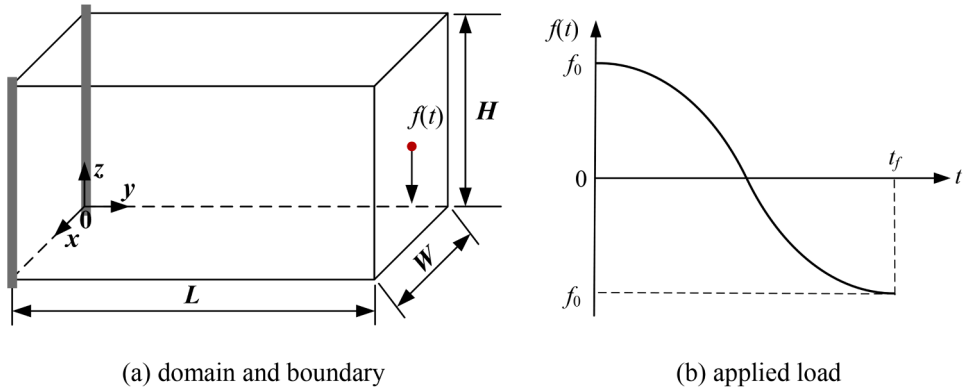

Fig. 7. Problem setup for the 3D cantilever beam.

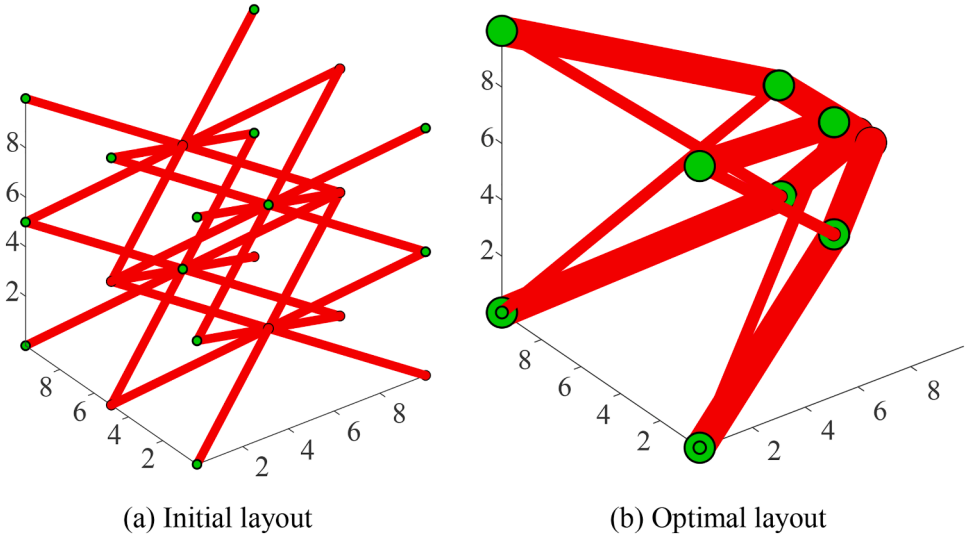

Fig. 8. Optimized spatially truss layout for the 3D cantilever beam.

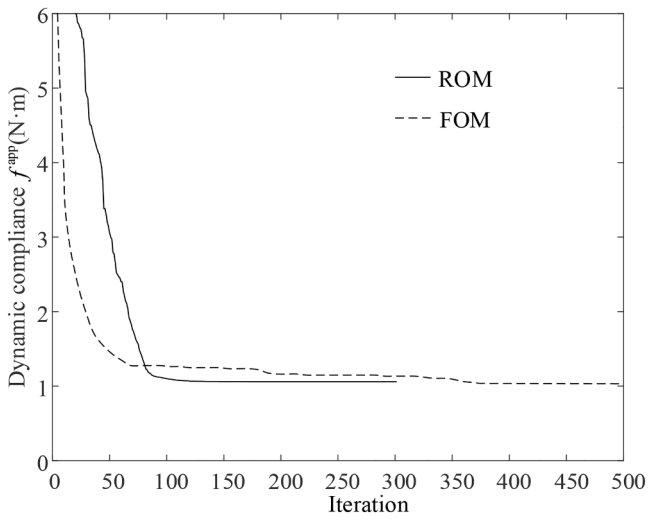

Fig. 9. Convergent histories for the 3D cantilever beam.

% to 0.04 % when e_b ranging from 10^{-4} to 10^{-6}. This implies that small tolerances result in better designs aligning with FOM. It is found that the corresponding speedup ratio varies from 3.15 to 2.13 falling within the acceptable range. Similarly, the storage requirement of the ROM is two orders of magnitude lower than that of the FOM. These implications are demonstrated in Table 2, which verifies the high efficiency of the proposed ROM in 3D spatial truss design problem.

5.3. Bridge design under moving load

This example intends to demonstrate how moving loads can be taken into account within the proposed algorithm. We consider a bridge of length $L = 16$m, height $H = 8$m, and thickness $h = 0.1$m, subjected to a moving load at a constant speed v with an amplitude of 10 kN, as illustrated in Fig. 10. Unlike in the previous examples, here we consider a passive region to represent the deck of the bridge. The background domain is discretized by 8×4 isogeometric plane stress elements with 10×6 control points. Each control point has two degrees of freedom, namely the displacements along the x and y directions. The material properties are the same as those described in Section 5.1. The number of sampling time step is $\bar{N} = 64$ with the time step, $\Delta t = 6.0$msand the prescribed tolerance for on-the-fly basis update is $e_b = 10^{-8}$.

Fig. 11 shows the initial layout and the optimal layouts of $v = 90$km/h and $v = 150$km/h. It is obvious that the truss element intersection occurs in the dotted circle domain, as plotted in Fig.11b and Fig.11c. As opposed to fixed load scenarios, the moving load results in the navigation of the truss elements across a broad space, which are prone to be overlapped or interlaced together. Thus, the reasonably optimized layout of truss is difficult to obtain without local geometry control. The truss intersection in the optimization process means geometrical interference of two truss elements, which makes the resulting optimal layout is unreasonable in the real truss structure. Although the truss elements are connected through the background grids, the truss intersection is not allowed such that local geometry control is introduced to address this issue.

In the context of moving load, the ground structure is applied to generate the initial layouts of truss and guarantee connectivity between truss elements. As plotted in Fig. 12, an enriched ground structure is selected as the initial layout, which is composed of repetitive lattice structures stacked together. Nevertheless, overlapped truss elements are connected by background grids, which can inherently prohibit truss elements from overlapping. Unlike the classic ground structure, the enriched ground structure introduces local node variables for exploring a more comprehensive design space.

Furthermore, as seen in Fig. 13a-b, when the vertex v_3 crosses over the edge $v_1 - v_2$, truss intersection occurs during the layout optimization, which is invalid from the perspective of engineering design. In terms of the work from Liu et al. [56], a local geometry control strategy is introduced to prevent truss elements from intersection. This strategy is to constrain the incircle radius of an arbitrary triangle in the enriched ground structure, as demonstrated in Fig.13c, which satisfies the following constraint,

$$R_i = \frac{2S_i}{P_i} \geq R_{\min}, i = 1, \cdots, m \tag{53}$$

where R_i, S_i and P_i denote, respectively, the inside radius, the area and the perimeter of the ith triangle, and $R_{\min}$ denotes allowable minimal inside radius.

To avoid dealing a large amount of inside radius constraints, we adopt the p-norm function to condense these local constraints. Thus, the constraint (53) is formulated as:

$$g_r = \left[\sum_{i=1}^{m} (R_{\min}/R_i)^p\right]^{1/p} - 1 \leq 0 \tag{54}$$

where m is the total number of triangles in the enriched ground structure and the coefficient p is set as 16 from Ref. [17].

Fig. 14 plots the optimized truss layout for the bridge problem with truss intersection constraint. The allowable minimal inside radii are the same and they are all 1.025 m for $v = 30$km/h, $v = 90$km/h and $v = 150$km/h. It is clear that the used ground structure with a local geometry control strategy is effective in obtaining the final reasonable layout of truss. This example further demonstrates the significance of dynamic topology optimization, which produces various truss layout designs with increasing velocity of moving load. This phenomenon arises because the moving load, as a spatiotemporally coupled excitation, induces the

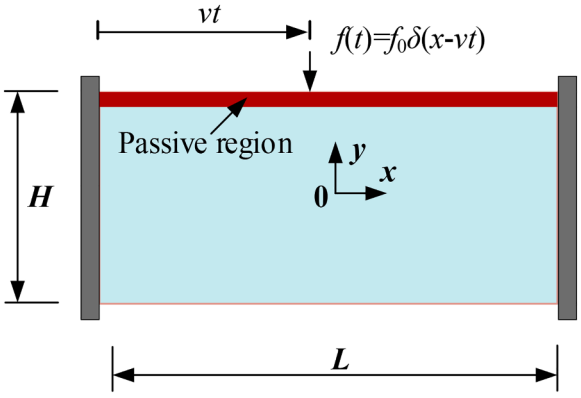

Fig. 10. Problem setup for the bridge problem.

Table 2
Performance comparison between FOM and ROMs with various e_b in optimal layout design of 3D cantilever beam.

Method	e_b	CPU running time/h	Speedup ratio	Optimal dynamic compliance/Nm	Memory requirement/Mb	Relative errors in optimal objective
FOM	-	98.05	1.00	1.0599	17,919.46	-
ROM	10^{-2}	20.04	4.89	3.5369	–	233.7 %
	10^{-4}	31.15	3.15	1.0591	–	0.07 %
	10^{-6}	42.50	2.31	1.0595	641.85	0.04 %

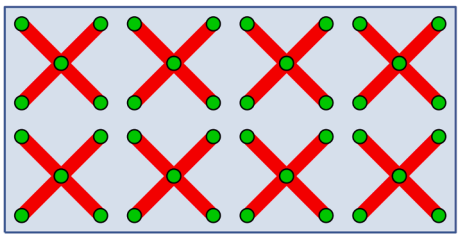

(a) Initial layout

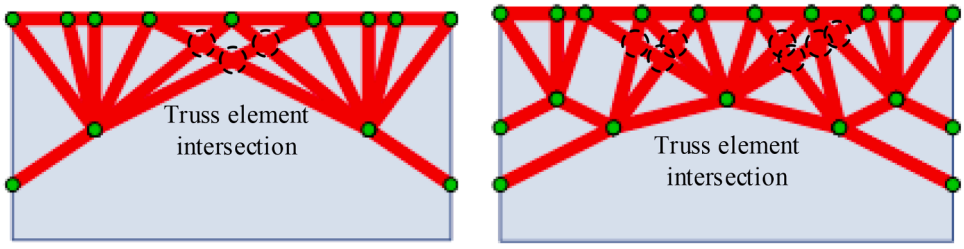

(b) Optimal layout for v=90km/h (c) Optimal layout for v=150km/h

Fig. 11. Optimized truss layout for the bridge problem without truss intersection constraint.

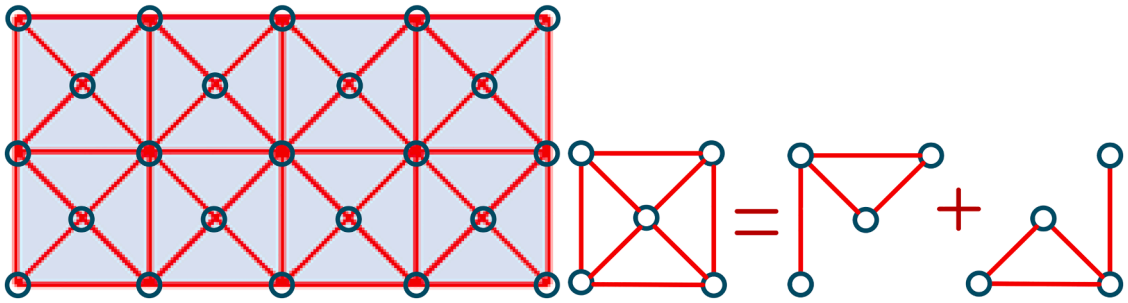

Fig. 12. Enriched ground structure.

participation of more structural modes in vibration as the load velocity increases. The dynamic effects of moving load affect the optimal layout and can't be captured by static optimization formulations.

Two main philosophies, Both FOM and Rom, make the objective function stably convergent to almost identical value, as depicted in Fig. 15.Next, we analyze the effect of different basis size using the scenario of v = 90km/h as an example. Table 3 illustrates that ROM remarkably reduces the computational time in contrast to FOM. When $N_b$increases, the speedup ratio decreases. Notably, only when a sufficient number of bases are used, accuracy for optimal dynamic compliance remains stable and reliable. As is known, the moving load behaves similarly to a frequency-sweeping load and can excite more modes to participate in the vibration. When N_b = 12, the optimal number of POD bases, the ROM achieves nearly the same objective value as the ROM, while requiring significantly less memory.

To verify the above hypothesis, we compare the displacement response at the midspan of the upper surface of the bridge, as shown in Fig. 16. when $N_b < 12$, the displacement response obtained by ROM significantly deviates from that obtained by FOM. This can be attributed to the fact that truncating higher-order modes can lead to significant computational errors. Thus, it is recommended to use N_b values in the range of 12 to 16. In fact, the minimal preferred number of POD bases is calculated as 12 from the inequality (A.8).

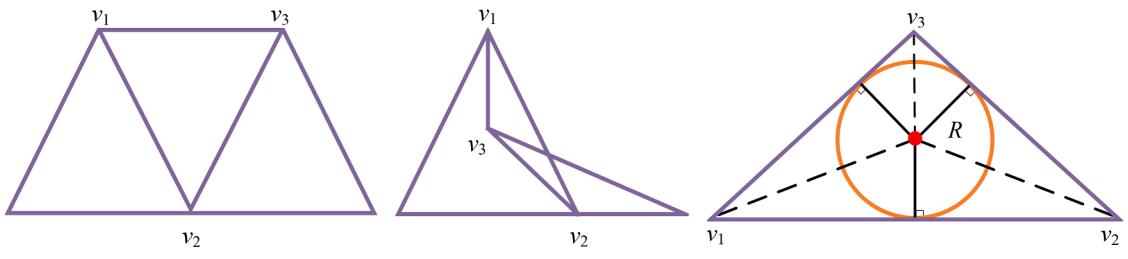

(a) Non-intersecting truss (b) Truss intersection (c) Incircle radius constraint

Fig. 13. Local geometry control to truss element intersection.

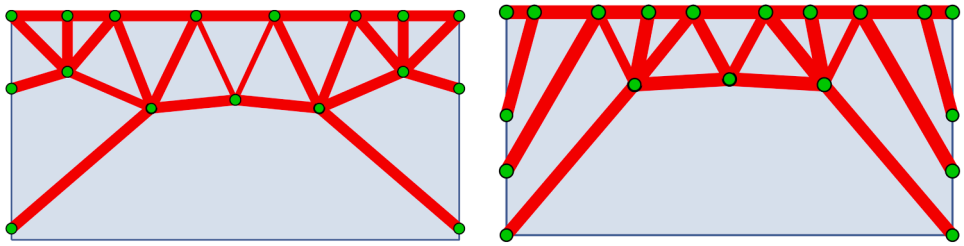

(a) Optimal layout for v=30km/h (b) Optimal layout for v=90km/h

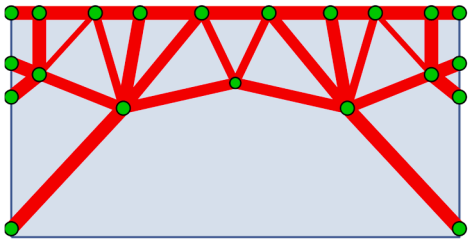

(c) Optimal layout for v=150km/h

Fig. 14. Optimized truss layout for the bridge problem with truss intersection constraint.

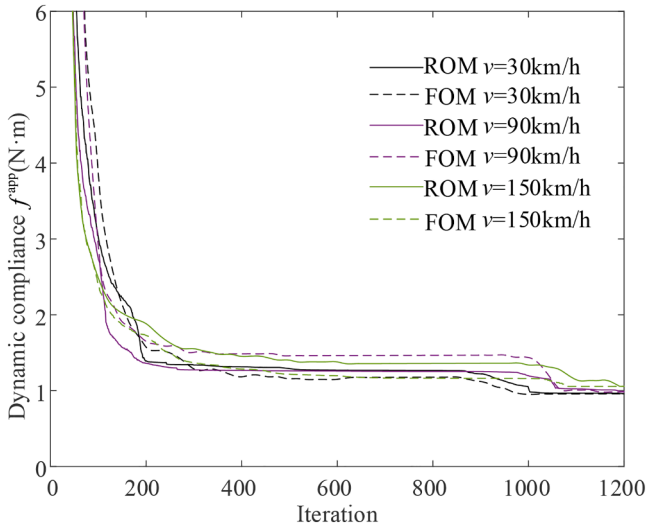

Fig. 15. Convergent histories for the bridge problem.

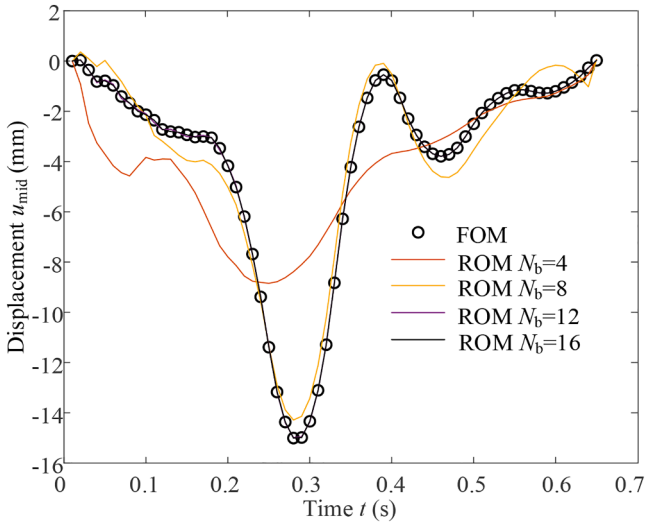

Fig. 16. Time histories of the vertical displacement at the top center for the bridge.

5.4. Limitations and extensions

While the proposed IGA-based SSM with on-the-fly POD ROM demonstrates high efficiency and accuracy for linear transient dynamic truss layout optimization under moving or time-dependent loads, this approach has some limitations. Strongly nonlinear behavior (e.g., geometric, material and contact nonlinearities) may require additional strategy including enrichment of the reduced basis and efficient computation of nonlinear terms. Extreme scenarios such as shock wave and strong multi-physics interaction, may increase the complexity of POD-based ROM. Future work will extend the methodology to nonlinear dynamic topology optimization of truss structures under intricate loading conditions, while preserving the compact representation and computational efficiency of ROM.

6. Conclusions

In this paper, the IGA-based SSM combined with POD is developed to

Table 3
Performance comparison between FOM and ROM with various N_b in optimal layout design of clamped bridge for the case of v = 90km/h.

Method	N_b	CPU running time/s	Speedup ratio	Optimal dynamic compliance/Nm	Memory requirement/Mb	Relative errors in optimal objective
FOM	-	720.782	1.00	0.9888	961.28	-
ROM	4	168.285	4.28	1.3756	-	39.1 %
	8	197.538	3.65	1.0702	-	8.2 %
	12	268.386	2.69	0.9991	31.60	1.0 %
	16	297.156	2.43	0.9889	-	0.01 %

mitigate the computational effort associated with transient dynamic topology optimization of truss. The IGA-based SSM can obtain the satisfactory optimal layout design of truss by arranging a small number of truss elements in the design domain. It addresses the challenge of dynamic truss layout optimization in a continuum. The POD procedure with incremental SVD is applied to construct the reduced unified basis for model reduction and on-the-fly dual reduction. On the other hand, to avoid the inconsistent error in the sensitivity evaluation, we construct the adjoint equation in the space-time discretized system based on the "discretize-then-differentiate" approach.

Two-dimensional and three-dimensional numerical examples on elastodynamic topology optimization of truss demonstrate the effectiveness of the proposed method in on-the-fly primal and dual reduction. We adopt a unified basis for the primal and dual problems, which achieves a good trade-off between accuracy and computational efficiency. As for scalability, the presented methodology employs element-by-element matrix–vector products and incremental SVD basis update. In addition, an enriched ground structure with a local geometry control strategy is introduced to address the truss element intersection issue during truss layout optimization under the moving loading. It can be concluded that the proposed method is an effective tool for transient truss optimization problem.

As a consequence, this work has potential to resolve large-scale 3D transient optimization problems of truss where storage is a bottleneck, and complex loading scenario like moving mass excitation. Further investigation is required to validate our conclusions across a more comprehensive spectrum of objective functions. In the future, the proposed method will be extended to the stiffener layout optimization or the lattice structure topology optimization subjected to a time-dependent load.

CRediT authorship contribution statement

Xiaoyan Teng: Methodology. **Lingzhi Li:** Software. **Xudong Jiang:** Writing – original draft, Methodology. **Haijiang Li:** Validation.

Declaration of competing interest

The authors declare the following financial interests/personal relationships which may be considered as potential competing interests Xiaoyan Teng reports financial support was provided by Foundation for Innovative Research Groups of the National Natural Science Foundation of China. If there are other authors, they declare that they have no known competing financial interests or personal relationships that could have appeared to influence the work reported in this paper.

Acknowledgments

This work was supported by the National Natural Science Foundation of China under Grant No 52271269, the Open project of National Key Laboratory of Ship Thermal Power under Grant No KJD231170, the Fundamental Research Funds for the Central Universities under Grant No AA6501, and the Guangdong Provincial Basic and Applied Basic Research Fund under Grant No 2022B1515250009.

Appendix A. Incremental singular value decomposition

As is well known, the resulting snapshot matrix conceivably increases to an intractable scale with the increasing time steps, especially for large-scale finite element model. To lessen the storage requirement to high-dimensional problem, an incremental SVD approach (Phalippou et al. [50]) is applied for economical acquisition of the POD bases.

Suppose we already have the rank-k truncated SVD of the first l columns of snapshot matrix$\mathbf{S}$:

$$\mathbf{S}_l \approx \mathbf{\Phi}_l \mathbf{\Sigma}_l \mathbf{\Psi}_l^{\mathrm{T}} \tag{A.1}$$

where $\mathbf{\Sigma}_l$ is a diagonal matrix with the k singular values of $\mathbf{S}_l$ in descending order along the main diagonal, $\mathbf{\Phi}_l$ and $\mathbf{\Psi}_l$ are the left and right singular matrices.

Owing to the low rank of $\mathbf{S}$, it is assumed that most vectors of $[\mathbf{u}_{l+1}, \mathbf{u}_{l+2}, \cdots, \mathbf{u}_{\overline{N}}]$ are linear dependent with the vectors in $\mathbf{\Phi}_l$. In general case, we suppose that the residuals of subsequent s vectors, $\mathbf{u}_{l+1}, \mathbf{u}_{l+2}, \cdots, \mathbf{u}_{l+s}$, are within the specified tolerance e_b when these s vectors are projected to the subspace spanned by $\mathbf{\Phi}_l$. But the residual of $\mathbf{u}_{l+s+1}$ is beyond the specified tolerance, that is,

$$\begin{aligned} &\| \mathbf{u}_i - \mathbf{\Phi}\mathbf{\Phi}^{\mathrm{T}}\mathbf{u}_i \| < e_b, i = l+1, \cdots, l+s \\ &\| \mathbf{u}_i - \mathbf{\Phi}\mathbf{\Phi}^{\mathrm{T}}\mathbf{u}_i \| > e_b, i = l+s+1 \end{aligned} \tag{A.2}$$

In terms of Eq. (A.1) and the above assumption, there is,

$$\begin{aligned} &\mathbf{S}_{l+s} = [\mathbf{S}_l, \mathbf{u}_{l+1}, \cdots, \mathbf{u}_{l+s}] \\ &\approx \left[\mathbf{\Phi}_l \mathbf{\Sigma}_l \mathbf{\Psi}_l^{\mathrm{T}} \mathbf{\Phi}_l \mathbf{\Phi}_l^{\mathrm{T}} \mathbf{u}_{l+1}, \cdots, \mathbf{\Phi}_l \mathbf{\Phi}_l^{\mathrm{T}} \mathbf{u}_{l+s}\right] \\ &= \mathbf{\Phi}_l \underbrace{\left[\mathbf{\Sigma}_l \mathbf{\Phi}_l^{\mathrm{T}} \mathbf{u}_{l+1} \cdots, \mathbf{\Phi}_l^{\mathrm{T}} \mathbf{u}_{l+s}\right]}_{\mathbf{Y}} \begin{bmatrix} \mathbf{\Psi}_l & \mathbf{0} \\ \mathbf{0} & \mathbf{I}_s \end{bmatrix}^{\mathrm{T}} \end{aligned} \tag{A.3}$$

where $\mathbf{I}_s$ is the s-order identity matrix.

We perform the SVD of $\mathbf{Y}$ and let $\mathbf{Y} = \mathbf{\Phi}_{\mathrm{Y}} \mathbf{\Sigma}_{\mathrm{Y}} \mathbf{\Psi}_{\mathrm{Y}}^{\mathrm{T}}$, where $\mathbf{\Psi}_{\mathrm{Y}}$ is split into $\mathbf{\Psi}_{\mathrm{Y}} = \begin{bmatrix} \mathbf{\Psi}_{\mathrm{Y}}^{(1)\mathrm{T}} & \mathbf{\Psi}_{\mathrm{Y}}^{(2)\mathrm{T}} \end{bmatrix}^{\mathrm{T}}$, and Eq. (A.3) can be rewritten as:

$$\mathbf{S}_{l+s} = \underbrace{\mathbf{\Phi}_l \mathbf{\Phi}_{\mathrm{Y}}}_{\mathbf{\Phi}_{l+s}} \underbrace{\mathbf{\Sigma}_{\mathrm{Y}}}_{\mathbf{\Sigma}_{l+s}} \underbrace{\begin{bmatrix} \mathbf{\Psi}_l \mathbf{\Psi}_{\mathrm{Y}}^{(1)} \\ \mathbf{\Psi}_{\mathrm{Y}}^{(2)} \end{bmatrix}^{\mathrm{T}}}_{\mathbf{\Psi}_{l+s}} \tag{A.4}$$

By comparison between Eq. (A.1) and Eq. (A.4), it is observed that the left singular matrices, $\mathbf{\Phi}_{l+s}$vs.$\mathbf{\Phi}_l$, share the common dimensionality, and the diagonal matrices, $\mathbf{\Sigma}_{l+s}$vs.$\mathbf{\Sigma}_l$, are the same case. We need a dynamically expandable storage matrix, $\mathbf{W} = \left[\mathbf{\Phi}_l^{\mathrm{T}} \mathbf{u}_{l+1} \cdots, \mathbf{\Phi}_l^{\mathrm{T}} \mathbf{u}_{l+s}\right]$. However, there is $k \ll N$for $\mathbf{W} \in \mathbf{R}^{k \times s}$, leading the low storage requirement.

From $(A.2)_2$, the residual of $\mathbf{u}_{l+s+1}$, $\mathbf{e}$, is defined as:

$$\mathbf{e} = \mathbf{u}_{l+s+1} - \mathbf{\Phi}_{l+s}\mathbf{\Phi}_{l+s}^{\mathrm{T}}\mathbf{u}_{l+s+1} \tag{A.5}$$

Let $p = \| \mathbf{e} \|$ and $\widetilde{\mathbf{e}} = \mathbf{e}/p$, and similarly, the SVD of $\mathbf{S}_{l+s+1}$ is constructed by

$$\begin{aligned}
&\mathbf{S}_{l+s+1} = [\mathbf{S}_{l+s}, \mathbf{u}_{l+s+1}] \\
&\approx \left[\mathbf{\Phi}_{l+s}\mathbf{\Sigma}_{l+s}\mathbf{\Psi}_{l+s}^{\mathrm{T}}p\widetilde{\mathbf{e}} + \mathbf{\Phi}_{l+s}\mathbf{\Phi}_{l+s}^{\mathrm{T}}\mathbf{u}_{l+s+1}\right] \\
&= [\mathbf{\Phi}_{l+s}, \widetilde{\mathbf{e}}] \underbrace{\begin{bmatrix} \mathbf{\Sigma}_{l+s} & \mathbf{\Phi}_{l+s}^{\mathrm{T}}\mathbf{u}_{l+s+1} \\ 0 & p \end{bmatrix}}_{\overline{\mathbf{Y}}} \begin{bmatrix} \mathbf{\Psi}_{l+s} & \mathbf{0} \\ 0 & 1 \end{bmatrix}^{\mathrm{T}}
\end{aligned} \tag{A.6}$$

Finding the SVD of $\overline{\mathbf{Y}}$, and letting $\overline{\mathbf{Y}} = \mathbf{\Phi}_{\overline{\mathbf{Y}}}\mathbf{\Sigma}_{\overline{\mathbf{Y}}}\mathbf{\Psi}_{\overline{\mathbf{Y}}}^{\mathrm{T}}$, then Eq. (A.6) is updated as:

$$\mathbf{S}_{l+s+1} \approx \underbrace{[\mathbf{\Phi}_{l+s}, \widetilde{\mathbf{e}}]\mathbf{\Phi}_{\overline{\mathbf{Y}}}}_{\mathbf{\Phi}_{l+s+1}} \underbrace{\mathbf{\Sigma}_{\overline{\mathbf{Y}}}}_{\mathbf{\Sigma}_{l+s+1}} \underbrace{\left(\begin{bmatrix} \mathbf{\Psi}_{l+s} & \mathbf{0} \\ 0 & 1 \end{bmatrix}\mathbf{\Psi}_{\overline{\mathbf{Y}}}\right)^{\mathrm{T}}}_{\mathbf{\Psi}_{l+s+1}} \tag{A.7}$$

From the Eqs. (A.1), (A.4) and (A.7), the incremental SVD technique enables the progressive updating of the POD basis. This on-the-fly update scheme makes it unnecessary to store snapshots across the time duration. It is sufficient to retain the reduced basis from the previous step along with a comparatively small diagonal matrix.

Notably, there exist a large number of nonzero but extremely small singular values. Without truncating these small singular values, the incremental SVD methodology may consume the huge computational cost. Therefore, we set a truncation threshold to determine the number of modes to retain with enough accuracy. The sufficiently few POD bases are selected in terms of the ratio of the total energy from the full-order space to that from the subspace.

$$I(r) = \sum_{i=1}^{r} \sigma_{\overline{N}i}^2 \Big/ \sum_{i=1}^{m} \sigma_{\overline{N}i}^2 \geq 99\% \tag{A.8}$$

where $\sigma_{\overline{N}i}$, $i = 1, \cdots, m$, represents the singular values of the snapshot matrix $\mathbf{S}$ and the minimal $r = \min[N_b]$ is the preferred number of POD bases.

Then, the reduced basis matrix $\mathbf{\Phi}$ is constructed by choosing the r columns of $\mathbf{\Phi}_{\overline{N}}$.

$$\mathbf{\Phi} = \mathbf{\Phi}_{\overline{N}}(:, i) i = 1, \cdots, r \tag{A.9}$$

According to the Eq. (A.9), the resultant reduced bases are employed to build reduced-order models with sufficiently fewer degrees of freedom, enabling efficient analysis and optimization of transient elastodynamic problems.

Appendix B. Details of sensitivity analysis

Substituting the HHT-α residual (16), the initial conditions (18), and the residual form of the Newmark-β FD relationships (22) into (23)-(24), we can acquire the dual variables as follows: for $t = \overline{N}$,

$$\begin{aligned}
&\boldsymbol{\mu}_{\overline{N}} = \partial f^{\mathrm{app}}/\partial \boldsymbol{\theta}_{\overline{N}}, \boldsymbol{\zeta}_{\overline{N}} = \mathbf{0} \\
&(\widehat{\mathbf{M}} + \gamma\Delta t\widehat{\mathbf{C}} + \beta\Delta t^2\widehat{\mathbf{K}})\boldsymbol{\lambda}_{\overline{N}} = -\beta\Delta t^2\boldsymbol{\mu}_{\overline{N}} - \gamma\Delta t\boldsymbol{\zeta}_{\overline{N}}
\end{aligned} \tag{B.1}$$

for $t = \overline{N} - 1, \cdots, 1$,

$$\boldsymbol{\mu}_t = \frac{\partial f^{\mathrm{app}}}{\partial \boldsymbol{\theta}_t} + \widehat{\mathbf{K}}\boldsymbol{\lambda}_{t+1} + \boldsymbol{\mu}_{t+1}, \boldsymbol{\zeta}_t = (\widehat{\mathbf{C}} + \Delta t\widehat{\mathbf{K}})\boldsymbol{\lambda}_{t+1} + \Delta t\boldsymbol{\mu}_{t+1} + \boldsymbol{\zeta}_{t+1} \tag{B.2}$$

$$\begin{aligned}
&(\widehat{\mathbf{M}} + \gamma\Delta t\widehat{\mathbf{C}} + \beta\Delta t^2\widehat{\mathbf{K}})\boldsymbol{\lambda}_t = \left[(1-\gamma)\Delta t\widehat{\mathbf{C}} + \left(\frac{1}{2} - \beta\right)\Delta t^2\widehat{\mathbf{K}}\right]\boldsymbol{\lambda}_{t+1} \\
&-\Delta t^2\left[\beta\boldsymbol{\mu}_t + \left(\frac{1}{2} - \beta\right)\boldsymbol{\mu}_{t+1}\right] - \Delta t[\gamma\boldsymbol{\zeta}_t + (1-\gamma)\boldsymbol{\zeta}_{t+1}]
\end{aligned} \tag{B.3}$$

for $t = 0$,

$$\begin{aligned}
&\widehat{\mathbf{M}}\boldsymbol{\lambda}_0 = \left[(1-\gamma)\Delta t\widehat{\mathbf{C}} + \left(\frac{1}{2} - \beta\right)\Delta t^2\widehat{\mathbf{K}}\right]\boldsymbol{\lambda}_1 \\
&-\left(\frac{1}{2} - \beta\right)\Delta t^2\boldsymbol{\mu}_1 - (1-\gamma)\Delta t\boldsymbol{\zeta}_1
\end{aligned} \tag{B.4}$$

As such, from the Eq. (B.1) to the Eq. (B.4), the adjoint equation can be solved backwards. Lagrange multiplier $\boldsymbol{\lambda}_t$, $t = \overline{N}, \cdots, 1, 0$ is calculated by LU decomposition.

Next, we calculate the partial derivatives, $\partial\widehat{\mathbf{R}}_t/\partial S_j$ from Eq. (18) for $t = 0$ and Eq. (16) for $t = 1, \cdots, \overline{N}$. They are, for $t = 0$,

$$\frac{\partial\widehat{\mathbf{R}}_t}{\partial S_j} = \frac{\partial\widehat{\mathbf{K}}}{\partial S_j}(\boldsymbol{\theta}_t + \beta_r\dot{\boldsymbol{\theta}}_t) + \frac{\partial\widehat{\mathbf{M}}}{\partial S_j}\left(\ddot{\boldsymbol{\theta}}_t + \alpha_r\dot{\boldsymbol{\theta}}_t\right) \tag{B.5}$$

for $t = 1, \cdots, \overline{N}$,

$$\frac{\partial \widehat{\mathbf{R}}_t}{\partial S_j} = \frac{\partial \widehat{\mathbf{K}}}{\partial S_j}\left[(1-\alpha)(\boldsymbol{\theta}_t + \beta_r \dot{\theta}_t) + \alpha(\boldsymbol{\theta}_{t-1} + \beta_r \dot{\theta}_{t-1})\right] + \frac{\partial \widehat{\mathbf{M}}}{\partial S_j}\left[\ddot{\theta}_t + \alpha_r((1-\alpha)\dot{\theta}_t + \alpha\dot{\theta}_{t-1})\right] \tag{B.6}$$

From Eqs. (2), (3) and (10), the partial derivatives, $\partial\widehat{\mathbf{K}}/\partial S_j$ and $\partial\widehat{\mathbf{M}}/\partial S_j$, are formulated as

$$\begin{aligned}
&\partial\widehat{\mathbf{K}}/\partial S_j = \boldsymbol{\Phi}^{\mathrm{T}}\partial\mathbf{K}_{ei}^{+}/\partial S_j\boldsymbol{\Phi} \\
&\partial\mathbf{K}_{ej}^{+}\Big/\partial S_j = \partial\mathbf{N}^{\mathrm{T}}\Big/\partial S_j\overline{\mathbf{K}}_{ej}\mathbf{N} + \mathbf{N}^{\mathrm{T}}\partial\overline{\mathbf{K}}_{ej}\Big/\partial S_j\mathbf{N} + \mathbf{N}^{\mathrm{T}}\overline{\mathbf{K}}_{ej}\partial\mathbf{N}\Big/\partial S_j \\
&\partial\overline{\mathbf{K}}_{ej}\Big/\partial S_j = \partial\mathbf{T}_{ej}^{\mathrm{T}}\Big/\partial S_j\mathrm{K}_{ej}^{*}\mathbf{T}_{ej} + \mathbf{T}_{ej}^{\mathrm{T}}\partial\mathrm{K}_{ej}^{*}\Big/\partial S_j\mathbf{T}_{ej} + \mathbf{T}_{ej}^{\mathrm{T}}\mathrm{K}_{ej}^{*}\partial\mathbf{T}_{ej}\Big/\partial S_j
\end{aligned} \tag{B.7}$$

$$\begin{aligned}
&\partial\widehat{\mathbf{M}}/\partial S_j = \boldsymbol{\Phi}^{\mathrm{T}}\partial\mathbf{M}_{ej}^{+}\Big/\partial S_j\boldsymbol{\Phi} \\
&\boldsymbol{\Phi}^{\mathrm{T}}\partial\mathbf{M}_{ej}^{+}\Big/\partial S_j = \partial\mathbf{N}^{\mathrm{T}}\Big/\partial S_j\overline{\mathbf{M}}_{ej}\mathbf{N} + \mathbf{N}^{\mathrm{T}}\partial\overline{\mathbf{M}}_{ej}\Big/\partial S_j\mathbf{N} + \mathbf{N}^{\mathrm{T}}\overline{\mathbf{M}}_{ej}\partial\mathbf{N}\Big/\partial S_j \\
&\partial\overline{\mathbf{M}}_{ej}\Big/\partial S_j = \partial\mathbf{T}_{ej}^{\mathrm{T}}\Big/\partial S_j\mathbf{M}_{ej}^{*}\mathbf{T}_{ej} + \mathbf{T}_{ej}^{\mathrm{T}}\partial\mathbf{M}_{ej}^{*}\Big/\partial S_j\mathbf{T}_{ej} + \mathbf{T}_{ej}^{\mathrm{T}}\mathbf{M}_{ej}^{*}\partial\mathbf{T}_{ej}\Big/\partial S_j
\end{aligned} \tag{B.8}$$

The derivatives of the stiffness and mass matrices for the truss element with respect to its cross-sectional area as follows:

$$\frac{\partial\mathbf{K}_{ej}^{*}}{\partial A_j} = \frac{E_r}{l_j}\begin{bmatrix} 1 & -1 \\ -1 & 1 \end{bmatrix}, \frac{\partial\mathbf{M}_{ej}^{*}}{\partial A_j} = \frac{\rho_r l_j}{6}\begin{bmatrix} 2 & 1 \\ 1 & 2 \end{bmatrix} \tag{B.9}$$

The derivatives of the stiffness and mass matrices for the truss element with respect to its nodal coordinates are as follows:

$$\frac{\partial\mathbf{K}_{ej}^{*}}{\partial x_{2j-1}} = -\frac{E_r A_j}{l_j^2}\frac{\mathrm{d}l_j}{\mathrm{d}x_{2j-1}}\begin{bmatrix} 1 & -1 \\ -1 & 1 \end{bmatrix}, \frac{\partial\mathbf{M}_{ej}^{*}}{\partial x_{2j-1}} = \frac{\rho_r A_j}{6}\frac{\mathrm{d}l_j}{\mathrm{d}x_j}\begin{bmatrix} 2 & 1 \\ 1 & 2 \end{bmatrix} \tag{B.10}$$

$$\frac{\partial\mathbf{K}_{ej}^{*}}{\partial y_{2j-1}} = -\frac{E_r A_j}{l_j^2}\frac{\mathrm{d}l_j}{\mathrm{d}y_{2j-1}}\begin{bmatrix} 1 & -1 \\ -1 & 1 \end{bmatrix}, \frac{\partial\mathbf{M}_{ej}^{*}}{\partial y_j} = \frac{\rho_r A_j}{6}\frac{\mathrm{d}l_j}{\mathrm{d}y_{2j-1}}\begin{bmatrix} 2 & 1 \\ 1 & 2 \end{bmatrix} \tag{B.11}$$

$$\frac{\partial\mathbf{K}_{ej}^{*}}{\partial x_{2j}} = -\frac{E_r A_j}{l_j^2}\frac{\mathrm{d}l_j}{\mathrm{d}x_{2j}}\begin{bmatrix} 1 & -1 \\ -1 & 1 \end{bmatrix}, \frac{\partial\mathbf{M}_{ej}^{*}}{\partial x_{2j}} = \frac{\rho_r A_j}{6}\frac{\mathrm{d}l_j}{\mathrm{d}x_{2j}}\begin{bmatrix} 2 & 1 \\ 1 & 2 \end{bmatrix} \tag{B.12}$$

$$\frac{\partial\mathbf{K}_{ej}^{*}}{\partial y_{2j}} = -\frac{E_r A_j}{l_j^2}\frac{\mathrm{d}l_j}{\mathrm{d}y_{2j}}\begin{bmatrix} 1 & -1 \\ -1 & 1 \end{bmatrix}, \frac{\partial\mathbf{M}_{ej}^{*}}{\partial y_{2j}} = \frac{\rho_r A_j}{6}\frac{\mathrm{d}l_j}{\mathrm{d}y_{2j}}\begin{bmatrix} 2 & 1 \\ 1 & 2 \end{bmatrix} \tag{B.13}$$

The derivative of the truss element length regarding its nodal coordinates are obtained as:

$$\begin{aligned}
&\mathrm{d}l_j/\mathrm{d}x_{2j-1} = \left(x_{2j-1} - x_{2j}\right)/l_j, \mathrm{d}l_j/\mathrm{d}x_{2j} = \left(x_{2j} - x_{2j-1}\right)/l_j \\
&\mathrm{d}l_j\Big/\mathrm{d}y_{2j-1} = \left(y_{2j-1} - y_{2j}\right)\Big/l_j, \mathrm{d}l_j\Big/\mathrm{d}y_{2j} = \left(y_{2j} - y_{2j-1}\right)\Big/l_j
\end{aligned} \tag{B.14}$$

where $l_j = \sqrt{\left(x_{2j} - x_{2j-1}\right)^2 + \left(y_{2j} - y_{2j-1}\right)^2}$ represents the truss element length.

Also, the sensitivities of the volume constraint regarding the nodal coordinates and the cross-sectional area of the truss element are given as follows:

$$\begin{aligned}
&\mathrm{d}V_{ej}/\mathrm{d}x_{2j-1} = A_j\mathrm{d}l_j/\mathrm{d}x_{2j-1}, \mathrm{d}V_{ej}\Big/\mathrm{d}y_{2j-1} = A_j\mathrm{d}l_j\Big/\mathrm{d}y_{2j-1} \\
&\mathrm{d}V_{ej}/\mathrm{d}x_{2j} = A_j\mathrm{d}l_j/\mathrm{d}x_{2j}, \mathrm{d}V_{ej}\Big/\mathrm{d}y_{2j} = A_j\mathrm{d}l_j\Big/\mathrm{d}y_{2j}
\end{aligned} \tag{B.15}$$

$$\mathrm{d}V_{ej}\,/\,\mathrm{d}A_j = l_j \tag{B.16}$$

The last piece of information required to fulfil the sensitivity analysis is associated with the partial derivatives, $\partial f^{\mathbf{app}}/\partial S_j$ and $\partial f^{\mathbf{app}}/\partial\mathbf{u}_t$, and we have

$$\partial f^{\mathbf{app}}/\partial S_j = 0, f^{\mathbf{app}}/\partial\mathbf{u}_t = \mathbf{F}_t/\overline{N} \tag{B.17}$$

Data availability

Some or all data, models, or codes that support the findings of this study are available from the corresponding author upon reasonable request.

References

[1] W.C. Dorn, Automatic design of optimal structures, J. Mec. 3 (1) (1964) 25–52.

[2] A. Bental, M.P. Bendsøe, A new method for optimal truss topology design, SIAM J. Optim. 3 (2) (1993) 322–358.

[3] M.P. Bendsøe, A. Bental, J. Zowe, Optimization methods for truss geometry and topology design, Struct. Optim. 7 (3) (1994) 141–159.

[4] Y. Lai, Q. Cai, Y. Li, J. Chen, Y.M. Xie, A new evolutionary topology optimization method for truss structures towards practical design applications, Eng. Struct 324 (2025) 119326.

[5] Y. Liu, Z. Wang, H. Lu, J. Ye, Y. Zhao, Y.M. Xie, An efficient optimisation approach for designing truss structures featuring a small number of modules, Eng. Struct. 328 (2025) 119757.

[6] Y. Liu, H. Hua, Z. Jia, L. Hovestadt, Generative design of hierarchical truss structures with desired stiffness and strength: recursive multiscale topology optimization based on powder bed fusion, Eng. Struct. 332 (2025) 120016.
[7] N. Sukulthanasorn, J. Xiao, K. Wagatsuma, R. Nomura, S. Moriguchi, K. Terada, A novel design update framework for topology optimization with quantum annealing: application to truss and continuum structures, Comput. Methods Appl. Mech. Engrg. 437 (2025) 117746.
[8] J. Li, Z. Wu, C. Xie, L. Xiao, A. Garg, G. Mei, The optimization design for the truss substructure of the novel truss-type submerged floating tunnel using the topology optimization method, Ocean Eng. 340 (2025) 122409.
[9] Q. Wang, W. Yang, L. Wang, G. Bai, G. Ma, Reinforcement design and structural performance for the topology optimized 3D printed concrete truss beams, Eng. Struct. 332 (2025) 120064.
[10] H. Lu, H.E. Fairclough, L. He, M. Gilbert, Combined truss and continuum topology optimization of structures, Struct. Multidisc. Optim. 68 (2025) 142.
[11] H.E. Fairclough, Adaptive member adding for truss topology optimization: application to elastic design, Struct. Multidisc. Optim. 67 (2024) 121.
[12] J. Zhou, Y. Zeng, G. Li, Size, shape and topology optimization of truss structure via the finite particle method, Comput. Struct. 305 (2024) 107570.
[13] G. Kozłowski, T. Sokół, Enhanced growth method for topology and geometry optimization of truss structures, Struct. Multidisc. Optim. 65 (2022) 220.
[14] P. Wei, H. Ma, M.Y. Wang, The stiffness spreading method for layout optimization of truss structures, Struct. Multidisc. Optim. 49 (4) (2014) 667–682.
[15] P. Hao, X. Yuan, C. Liu, B. Wang, H. Liu, G. Li, F. Niu, An integrated framework of exact modeling, isogeometric analysis and optimization for variable-stiffness composite panels, Comput. Methods Appl. Mech. Eng. 339 (2018) 205–238.
[16] Y. Sun, Y. Zhou, Y. Shi, H. Li, K. Tian, B. Wang, Isogeometric-analysis-based stiffness spreading method for truss layout optimization, Comput. Methods Appl. Mech. Eng. 390 (2022) 114455.
[17] Y. Sun, Y. Zhou, Z. Ke, K. Tian, B. Wang, Stiffener layout optimization framework by isogeometric-based stiffness spreading method, Comput. Methods Appl. Mech. Eng. 390 (2022) 114348.
[18] H. Zhang, W. Zhang, Shape-topology-layout optimization of stiffened shell structures via the feature-driven Optimization (FDO) method, Comput. Methods Appl. Mech. Eng. 452 (2026) 118771.
[19] G. Shi, Z. Liu, D. Lu, X. Du, Q. Zhang, Analysis method for impact mechanical response and failure mode of cable truss structure, Thin Wall. Struct. 215 (2025) 113438.
[20] P. Lehner, M. Krejsa, P. Pařenica, V. Křivý, J. Brožovský, Fatigue damage analysis of a riveted steel overhead crane support truss, Int. J. Fatigue 128 (2019) 105190.
[21] S.J. Salt, A.G. Weldeyesus, M. Gilbert, J. Gondzio, Layout optimization of pin-jointed truss structures with minimum frequency constraints, Eng. Optim. 55 (8) (2022) 1403–1421.
[22] S. Ma, J. Mareček, Vyacheslav Kungurtsev & Marek Tyburec, truss topology design under harmonic loads peak power minimization with semidefinite programming, Struct. Multidisc. Optim. 68 (2025) 40.
[23] O. Giraldo-Londoño, G.H. Paulino, PolyDyna: a Matlab implementation for topology optimization of structures subjected to dynamic loads, Struct. Multidisc. Optim. 64 (2021) 957–990.
[24] F.J. Ramírez-Gil, E.C.N. Silva, W. Montealegre-Rubio, Design of topology-optimized functionally graded porous structures under transient loads, Int. J. Mech. Sci. 284 (2024) 109732.
[25] S. Mukherjee, D. Lu, B. Raghavan, P. Breitkopf, S. Dutta, M. Xiao, W. Zhang, Accelerating largescale topology optimization: stateoftheart and challenges, Arch. Comput. Methods Eng. 28 (2021) 4549–4571.
[26] Q. Li, O. Sigmund, J.S. Jensen, N. Aage, Reduced-order methods for dynamic problems in topology optimization: a comparative study, Comput. Methods Appl. Mech. Eng. 387 (2021) 114149.
[27] J. Li, Y. Zhang, Z. Du, C. Liu, W. Zhang, X. Guo, X. Guo, A moving morphable component-based topology optimization approach considering transient structural dynamic responses, Int. J. Numer. Methods Eng. 123 (3) (2022) 705–728.
[28] Y. Zhu, Z. Kang, An efficient transient dynamic topology optimization framework based on successive iteration of analysis and design, Comput. Methods Appl. Mech. Eng. 421 (2024) 116787.
[29] H. Ding, B. Xu, C. Huang, Z. Duan, A multi-scale discrete material optimization model for optimization of structural topology and material orientations to minimize dynamic compliance, Struct. Multidisc. Optim. 64 (2021) 1343–1565.
[30] K. Ege, X. Boutillon, B. David, High-resolution modal analysis, J Sound Vib. 325 (2009) 852–869.
[31] X. Wang, X. Chen, K. Long, B. Wang, Dynamic topology optimization of seismic structure based on model reduction method. Engineering Mechanics. https://link.cnki.net/urlid/11.2595.O3.20240722.1145.002.
[32] Y. Li, X. Wei, H. Cao, H. Bai, B. Wang, P. Hao, An adaptive model reduction method for harmonic response analysis of non-proportional damping structures, J. Solid Rocket Technol. 46 (3) (2023) 352–358.
[33] K. Long, X. Yang, N. Saeed, R. Tian, P. Wen, X. Wang, Topology optimization of transient problem with maximum dynamic response constraint using SOAR scheme, Front. Mech. Eng. 16 (2021) 593–606.
[34] H. Kristiansen, N. Aage, An open-source framework for large-scale transient topology optimization using PETSc, Struct. Multidisc. Optim. 65 (10) (2022) 295.
[35] H.S. Koh, G.H. Yoon, Large-scale topology optimization for dynamic problems using a repetitive substructuring approach, Struct. Multidisc. Optim. 67 (2024) 33.
[36] L. Xu, W. Zhang, W. Yao, S. Youn, X. Guo, Machine learning accelerated MMC-based topology optimization for sound quality enhancement of serialized acoustic structures, Struct. Multidisc. Optim. 67 (2024) 85.
[37] H. Ma, K. Xiao, Y. Huang, S. Duan, Y. Li, Daining Fang, structural transient dynamic topology optimization based on autoencoder-enhanced generative adversarial network and elitist guidance evolutionary algorithm, Comput. Methods Appl. Mech. Engrg. 447 (2025) 118417.
[38] N. Sukulthanasorn, K. Terad, Quantum neural network-assisted topology optimization: concept and implementation with parameterized quantum circuits, Comput. Methods Appl. Mech. Engrg. 448 (2026) 118411.
[39] A.Z.B. Nejad, M.M. Sahebi, An investigation on the capability of proper orthogonal modes in determining the natural frequencies and damping ratios of linear structural systems, Eng. Struct. 243 (2021) 112691.
[40] C.E.N. Mazzilli, P.B. Gonçalves, R. Guilherme, Franzini. Reduced-order modelling based on non-linear modes, Int. J. Mech. Sci. 214 (2022) 106915.
[41] S. Liang, Z.H.A.N.G. Lei, H. Wang, Yanyan Wang, 1D high order dynamic modeling method of thin-walled beam with fillet cross-section based on principal component analysis, J. Vibrat. Shock. 42 (07) (2023) 187–193.
[42] Y. Nakamura, S. Sato, N. Ohnishi, Application of proper orthogonal decomposition to flow fields around various geometries and reduced-order modeling, Comput. Methods Appl. Mech. Eng. 432 (2024) 117340.
[43] H. Wang, K. Lu, J. Liu, J. Tong, W. Zheng, K. Zhang, Fast solution of underwater vehicle vibration response based on POD method, J. Nanjing Univ. Aeronaut. Astronaut. 56 (6) (2024) 1066–1073.
[44] Y. Yang, X. Zhao, Q. Cheng, R. Guo, M. Li, J. Zhou, POD-ANN as digital twins for surge line thermal stratification, Nucl. Eng. Des. 428 (2024) 113487.
[45] Z. Ke, Y. Shi, P. Zhang, K. Tian, B. Wang, Vibration reduction optimization of complex thin-walled structures based on global POD reduced-order model, Acta Aeronaut. Et Astronaut. Sin. 44 (13) (2023) 148–163.
[46] M. Xiao, D. Lu, P. Breitkopf, B. Raghavan, S. Dutta, W. Zhang, On-the-fly model reduction for large-scale structural topology optimization using principal components analysis, Struct. Multidisc. Optim. 62 (2020) 209–230.
[47] S. Li, J. Yin, D. Guo, G. Li, H. Wang, An efficient online successive reanalysis method for dynamic topology optimization, Adv. Eng. Softw. 191 (2024) 103625.
[48] D. Cao, Y. Zeng, Z. Meng, G. Li, A transient dynamic topology optimization method with approximate dynamic response sensitivity using equivalent static loads, Comput. Methods Appl. Mech. Eng. 436 (2025) 117760.
[49] K. Yan, D. Liu, J. Yan, Topology optimization method for transient heat conduction using the Lyapunov equation, Int. J. Heat Mass Transf. 231 (2024) 125815.
[50] P. Phalippou, S. Bouabdallah, P. Breitkopf, P. Villon, M. Zarroug, On-the-fly' snapshots selection for Proper Orthogonal decomposition with application to nonlinear dynamics, Comput. Methods Appl. Mech. Eng. 367 (2020) 113120.
[51] M. Xiao, J. Ma, X. Gao, P. Breitkopf, B. Raghavan, W. Zhang, L. Cauvin, P. Villon, Primal–dual on-the-fly reduced-order modeling for large-scale transient dynamic topology optimization, Comput. Methods Appl. Mech. Engrg. 428 (2024) 117099.
[52] J. Chung, G.M. Hulbert, A time integration algorithm for structural dynamics with improved numerical dissipation-the generalized-α method, J. Appl. Mech. 60 (1993) 371–375.
[53] J.S. Jensen, P.B. Nakshatrala, D.A. Tortorelli, On the consistency of adjoint sensitivity analysis for structural optimization of linear dynamic problems, Struct. Multidisc. Optim. 49 (5) (2014) 831–837.
[54] X. Jiang, W. Zhang, Xiaoyan Teng and Xiangyang Chen, concurrent topology optimization of multi-scale composite structures subjected to dynamic loads in the time domain, Mathematics 11 (16) (2023) 3488.
[55] R.A. Waltz, J.L. Morales, J. Nocedal, D. Orban, An interior algorithm for nonlinear optimization that combines line search and trust region steps, Math. Program. 107 (2006) 391–408.
[56] J.L. Ma, Truss-like structure design with local geometry control, Comput. Aided Des. Appl. 14 (3) (2017) 324–330.